Comprehensive Biomechanical Analysis of Canine Orthopedics: Evaluation of Patellar Tendon, Radius and Ulna Fractures, and Post-Screw Removal Stress

犬の整形外科におけるバイオメカニクス分析：

膝蓋腱、橈骨・尺骨骨折、スクリュー抜去後のストレスの評価

JOINT GRADUATE SCHOOL OF VETERINARY MEDICINE

YAMAGUCHI UNIVERSITY

DITO ANGGORO

SEPTEMBER 2024

TABLE OF CONTENT

LIST OF TABLES

LIST OF FIGURES

ABSTRACT

Orthopedic injuries in small animal patients represent a considerable concern within veterinary medicine, influencing their overall well-being and functional capacity. Among these injuries, patellar tendon (PT) and bone fractures can result in reduced mobility, producing discomfort and restricting their capacity to participate in regular physical activities. In particular, the phase of removing screws after a surgical procedure might also potentially cause unexpected stress on the skeletal system, affecting the overall effectiveness of orthopedic treatments. The current studies delve into the complex biomechanical aspects of small animal orthopedics, specifically focusing on prevalent issues involving tendons and bones.

The first chapter quantitatively evaluates the biomechanical and viscoelastic properties of the dog PT under the influence of neuromuscular blocking agents (NMBA), particularly at varying stifle angles. This study not only investigates into the biomechanics of the dog PT but also aims to establish a standard reference and introduce a novel examination method for this crucial anatomical structure. Diagnosing dog PT disorders in clinical practice involves various methods, including radiography, magnetic resonance imaging (MRI), and elastography. However, these instrument's availability and dependability often depend on laboratory settings, non-quantitative analysis methods, and operator skills or experience. Alternatively, myotonometric methods have been widely employed in human tendon evaluation and have emerged as a promising approach for dog PT assessment. This approach presents several advantages, including portability, non-invasiveness, and high reliability. By integrating this evaluation into the comprehensive biomechanical testing methodologies employed in the study, the research aims to provide a more thorough understanding of the complex responses of the PT. The method not only helps to advance scientific knowledge but also has the potential to

improve diagnostic precision and assist clinicians in optimizing treatment strategies for tendon-related conditions.

The second chapter employs finite element analysis (FEA) to elucidate fracture mechanisms within the radius and ulna of toy breed dogs. This computational approach allows for a detailed examination of stress distribution patterns during the fracture condition, offering a deeper comprehension of small animal orthopedics. To the best of our knowledge, no studies have investigated fracture mechanisms in toy breed dogs utilizing FEA, especially in toy poodles. The insights from this novel approach fill a critical gap in existing research, providing valuable information that could significantly impact veterinary surgery practices. While FEA is widely used in human medicine to study radius ulna fractures, its application in veterinary orthopedics remains limited. The evolving potential of FEA in veterinary orthopedics holds promise for addressing a range of complex challenges, offering insights into tissue deformation, stress distribution, and other biomechanical aspects. Moreover, the FEA method provides an alternative substitute for directly investigating these phenomena in living dog experiments, which could present ethical obstacles. The limitation underscores the significance of utilizing computational models to advance understanding of fracture dynamics, contributing to more informed and ethically sound approaches to diagnosing and treating fractures in toy-breed dogs. The implications of this research would potentially influence veterinary orthopedics and the broader field of animal welfare.

The third chapter extends our investigation into veterinary orthopedic implants by examining post-screw removal stress in the toy poodle radius. The research was prompted by the recognition of complications associated with screw removal, with a particular emphasis on reported occurrences of refracture in the radius. The primary objective is to contribute valuable insights into the biomechanical implications of screw arrangements on post-operative screw removal on bone stress distribution in dog radius fractures. Notably, our study addresses a gap

in existing research, as there have been no prior examinations of stress distribution on the toy poodle radius after screw removal using FEA. Treating radius fractures in toy poodle dogs is a complex clinical challenge due to their small size, unique bone structure, and limited blood supply. Innovative approaches were necessary for effective treatment and optimal post-operative outcomes. Implementing the revolutionary impact of FEA in biomedical engineering, our methodology plays a pivotal role in predicting biological responses to mechanical stimuli and efficiently analyzing tissue deformation and stress distribution. This insightful knowledge significantly enhances the understanding of the stress distribution related to the removal of the screw after surgery, providing essential insights for more informed clinical decision-making.

As these chapters coalesce, the dissertation aims to provide a comprehensive foundation of knowledge that advances the understanding of small animal musculoskeletal biomechanics and shapes the future landscape of surgical interventions in veterinary orthopedics. The outcome of this research suggests considerable promise for improving the overall well-being and health outcomes of companion animals.

GENERAL INTRODUCTION

Exploring the complexities of small animal orthopedics in veterinary medicine requires thoroughly examining biomechanics to improve the understanding of musculoskeletal disorders and enhance treatment approaches. The present work investigates a comprehensive examination of the biomechanical and viscoelastic characteristics of the patellar tendon, fractures occurring in the one-third distal radius of toy breed dogs, and the resulting stress following the removal of screws in bone implant surgeries.

Patellar tendon (PT)

The PT comprises collagen fibers, elastin, and proteoglycans. The primary function of the PT is to facilitate the extension of the stifle joint during weight-bearing activities or transmitting forces generated by the quadriceps muscles during ambulation (Wheatley et al. 2020). Any disruption or alteration in this dense fibrous structure's biomechanical and viscoelastic properties can profoundly impact a dog's ability to move and maintain stability. The patellar tendon has a remarkable ability to store and release mechanical strain energy due to its biomechanical properties and the strategic utilization of the force-length-velocity dynamics of muscle fibers (Mersmann et al. 2019). The combination of these biomechanical characteristics not only improves the overall stability of the musculoskeletal system but also maximizes the performance and functionality of the associated muscles, illustrating an adequate adaptation to the physiological requirements of mechanical stress in the extremities. In addition, tendons might adapt to different loads by increasing their stiffness through changes in their material properties and undergoing radial development over an extended period (Bohm et al. 2015). During regular movement, tendons experience dynamic loading, resulting in a response that varies over time. This dynamic loading exhibits a nuanced response from the

tendinous tissues, a phenomenon strongly linked to their unique viscoelastic properties. As highlighted by (Kneifel et al. 2023) the time-dependent deformation and stress relaxation inherent in the viscoelastic nature of tendons play a crucial role in shaping their adaptation to mechanical stimuli over time. Understanding these complexities is crucial for furthering the comprehension of physiological processes and the development of targeted treatments for musculoskeletal disorders.

Patellar tendon assessment

Numerous studies have investigated the biomechanical and viscoelastic properties of the animal PT. One study on ex vivo testing of dog patella-ligament-tibia (PLT) segments explored the relationship between donor size, PLT dimensions, and graft mechanical properties (Biskup et al. 2014). Further research examined mechanical damage to PT using ultrashort echo (UTE) MRI (Pownder et al. 2021), while (Torniainen et al. 2019) explored the mechanical properties of PT using near-infrared spectroscopy (NIRS). In clinical practice, shear wave elastography is widely recognized as the primary method for examining the patellar tendon due to its simplicity (Berko et al. 2015; McCagherty et al. 2020; Kuervers et al. 2021; Hardy et al. 2017; Pearson et al. 2017). In bridging the gap between exploring various assessment methods for PT, researchers have also addressed the myotonometric approach. This method has found extensive application in the assessment of human musculoskeletal features, particularly in the evaluation of the PT, Achilles tendon (AT), and viscoelastic muscles (Liu et al. 2018; Pozarowszczyk et al. 2017; Young et al. 2018; Chen et al. 2019; Klich et al. 2020). The evaluation process relies on the oscillation theory, wherein multiple mechanical impulses are applied to soft tissue, and the reflected energy is measured to gauge the tissue's viscoelastic properties. Notably, the myotonometric device boasts several advantages, including portability,

non-invasiveness, painlessness, and high reliability (Schneebeli et al. 2020; Bravo-Sánchez et al. 2022).

Neuromuscular Blocking Agents (NMBA)

The primary objective of NMBA is to achieve muscle immobilization, facilitate surgical procedures, and mitigate the risks associated with uncontrolled muscle movements (Popovici et al. 2014). This drug works by temporarily inhibiting acetylcholine receptors, disrupting the transmission of nerve impulses to muscle fibers, and inducing a reversible state of paralysis (Motamed, 2023). Rocuronium has been reported as a non-depolarizing NMBA commonly utilized in veterinary medicine (Martin-Flores et al. 2018). While existing research sheds light on NMBA effects on muscle physiology (Alderson et al. 2007; Dugdale MA et al. 2002; Auer 2007), its specific impact on tendons remains not fully understood. Understanding potential changes in tendon stiffness, elasticity, and viscoelastic properties is essential for small animal practice. Moreover, the influence of NMBAs on tendons may vary with joint angles, reflecting the dynamic nature of joint movement during different activities. Given the complex interplay, it was a nuanced exploration beyond the current scope of veterinary literature.

Fractures on one-third distal radius

Toy-breed dogs have become extremely popular as pets in households. According to a survey by ANICOM (the Japanese animal insurance business) in 2023, toy poodles were ranked among the top five preferred dog breeds in Japan. Nevertheless, their small size gives rise to intrinsic weaknesses, especially in their skeletal structure (Boudrieau R.J. 2003; McCartney et al. 2010). Small breed dogs have distinct variations in the lengths and diameters of their forelimbs compared to large breed dogs, as observed from an anatomical perspective. As indicated by (Aikawa et al. 2018; Brianza et al. 2006; Brianza et al. 2007; Welch et al.

1997) the unique physical characteristics of toy poodles distal antebrachium, such as their small size, specific bone structure, and limited blood flow, present challenges when treating fractures in these dogs. Meanwhile, fractures in the proximal radius were infrequent due to the protective effect of the nearby muscles, and the less rigid lateral epicondylar crest is more prone to fracturing before the radius (Bruce WJ 2006). A study conducted by (Bell et al. 2022) showed that the most common scenarios leading to fractures in these small animal companions involved falls from considerable heights. These situations can occur during routine activities, such as being carried by a caregiver or attempting to navigate household structures like sofas or staircases. Effectively managing radius fractures in toy poodles presents a complex clinical challenge, necessitating innovative approaches to ensure successful treatment and positive post-operative outcomes.

Bone implant

The use of plates and screws as bone implants has become a standard practice in veterinary orthopedics to provide stability and support during the healing process. Locking compression plates (LCPs) have emerged as a prominent and preferred choice for effectively addressing fractures, offering stability and accelerated healing. Prior research has pointed out the advantages of LCPs, such as the ability to select different screw types, protect the crucial blood supply, and obtain optimal stability by utilizing screws at various angles (Alwen et al., 2018; Gibert et al., 2015; (Alwen et al. 2018; Gibert et al. 2015; Haaland et al. 2009). However, numerous post-operative complications have been documented following the removal of screws, with a notable prevalence of refracture observed in the radius of dogs (Aikawa et al. 2018; De Arburn Parent et al. 2017; Haaland et al. 2009). These complications underscore the importance of careful consideration and precise surgical techniques involving screw removal, as the risk of refracture poses a significant concern for the overall success of the intervention.

Notably, emerging evidence suggests that the plate size and arrangement of screws during the surgical process might have a positive correlation with the overall success rate of the operation (Wang et al. 2020). Optimal screw placement, considering factors such as size, position, and orientation, plays a crucial role in achieving structural stability and reducing the risk of complications post-removal (Largura et al. 2014; Bologna et al. 2023).

Finite Element Analysis (FEA)

The influence of FEA in the field of biomedical engineering is readily apparent due to its exceptional capacity to investigate intricate problems. This method allows researchers to simulate and analyze complex bone mechanics by breaking down structures into smaller and manageable elements (Ruffoni and Van Lenthe 2017). In particular, FEA uses a numerical approach to provide detailed insights into bone behavior under different conditions, surpassing the limitations of experimental methods. It serves as an ethical and practical alternative to direct experimentation on live animals in biomedical engineering, predicting fracture patterns, assessing implant materials, and optimizing surgical procedures (Johnson and Troy 2017; Pramudita et al. 2022; Revel et al. 2020; Yamazaki et al. 2021). The approach has played a pivotal role in deepening understanding of bone stress distribution, deformation patterns, and potential failure points. While FEA has been extensively researched in human medicine, its potential remains largely unexplored in veterinary medicine. Limited awareness and expertise in computational modeling within the veterinary community contribute to this gap, hindering the widespread use of advanced computational tools in veterinary research and practice. Therefore, bridging this gap could unlock new possibilities for implementing advanced computational tools in veterinary studies, enhancing understanding of animal bone behavior and leading to innovative methods for addressing musculoskeletal disorders in different species.

STUDY OBJECTIVE

The research comprehensively evaluates biomechanical and viscoelastic attributes in small animal orthopedics. In particular, the study investigates the effects of NMBA and various knee loading angles (normal, flexion, and extension) on dog PT. Additionally, it explores the heightened susceptibility of toy poodles to the distal radius and ulna fractures and biomechanical issues with post-operative screw removal. This inquiry aims to enhance understanding of dog musculoskeletal biomechanics, contributing to advancements in small animal diagnostic and therapeutic methods.

CHAPTER I

Quantitative evaluation of the biomechanical and viscoelastic properties of the dog patellar tendon in response to neuromuscular blockade at different stifle angles

This work has been published as follows:

Anggoro, D, Purba, M.S., Nishida, N., Itoh, H., Itamoto, K., Nemoto, Y., Munekazu, N., Sunahara, H., and Tani, K. (2024). Quantitative evaluation of the biomechanical and viscoelastic properties of the dog patellar tendon in response to neuromuscular blockade at different stifle angles. *PLoS ONE*, 19(1): e0292453. https://doi.org/10.1371/journal.pone.0292453. PMID: 38166027. PMCID: PMC10760779.

1.1. Abstract

The patellar tendon (PT) is crucial for maintaining stability and facilitating movement in the stifle joint. Elastography has been recognized as a prominent method for evaluating PT properties in humans and dogs. The utilization of oscillation methods in canine studies remains limited despite their extensive documentation in human studies. Our study represents the first effort to quantitatively assess and compare the effects of muscle relaxants on the biomechanical and viscoelastic characteristics of the PT at varying stifle angles in living dogs. Five healthy female beagles were used in this study. Biomechanical (tone, stiffness, and decrement) and viscoelastic (relaxation time and creep) properties of the PT were measured using MyotonPRO (Myoton Ltd, Estonia) before and following administration of rocuronium (0.5 mg/kg/body weight) at normal, extended, and flexed positions. Rocuronium was selected for its safety, controllability, and widespread clinical use in veterinary anesthesia. Two-way analysis of variance showed that tone, stiffness, and decrement were significantly higher ($P < 0.001$) in the control group than in the muscle relaxation group. At the same time, relaxation time and creep were significantly lower ($P < 0.001$) in the control group than in the muscle relaxation group. The findings indicate that stifle angle position and muscle rexalant administration fundamentally alter the biomechanical loading conditions of the PT, leading to changes in its viscoelastic properties. Therefore, this novel quantitative data could benefit clinical settings that necessitate accurate and objective methods for risk identification and monitoring PT biomechanics in dogs.

1.2. Introduction

Tendons are mechanical cushions that transmit and absorb force when jumping and landing. Tendons also contribute to storing and releasing energy, which helps muscles

function more effectively (Liu et al. 2018). Knee extensors comprise the quadriceps muscle and tendon, medial and lateral patellar retinaculum, patella, patellar tendon (PT), and tibial tubercle (LaPrade et al. 2018). The PT also plays a crucial role in transferring the force from the quadriceps to the tibia (Wheatley et al. 2020). The proximal attachment (inferior pole) is mainly affected if the PT becomes inflamed from constant strain. Meanwhile, the superior pole of the patella (quadriceps tendon insertion) and tibial tuberosity (patellar tendon distal attachment) are rarely affected by strain (Wadugodapitiya et al. 2021). Hence, accurately assessing tendon properties may be a valuable addition to the standard tests to evaluate skeletal muscle function.

Numerous methods for diagnosing canine PT disorders, including radiography, magnetic resonance imaging (MRI), and elastography, are used in clinical practice. Radiography may reveal soft tissue edema, irregular margins, and the PT's thickening at the tibial tuberosity level. Meanwhile, MRI and elastography provide better accuracy and image quality when diagnosing injuries due to their superior visualization of soft tissues (Piccionello et al. 2018). However, the availability and dependability of these modalities depend on the laboratory settings, non-quantitative analysis methods, and operator skills or experience. Alternatively, myotonometric medicine has been widely used in human evaluation to evaluate the PT, Achilles tendon (AT), and viscoelastic muscles (Liu et al. 2018; Pozarowszczyk et al. 2017; Young et al. 2018; Chen et al. 2019; Klich et al. 2020). Myotonometric evaluations are based on the oscillation theory that involves the application of several mechanical impulses to soft tissue and measuring the reflected energy, representing the tissue's viscoelastic properties. The device has several advantages: it is portable, non-invasive, painless, and highly reliable (Schneebeli et al. 2020; Bravo-Sánchez et al. 2022).

Neuromuscular blocking agents (NMBA) are frequently used to improve skeletal muscle relaxation during surgery that requires general anesthesia. Rocuronium is an example of a non-depolarizing NMBA frequently used in veterinary clinical practice because of its ability to induce muscle paralysis while reducing stiffness. Rocuronium relaxes the muscles by acting on nerve endings and inhibiting the release of acetylcholine. Additionally, rocuronium improves tendon gliding and joint movement, resulting in a safer and more efficient surgery (Martin-Flores et al. 2018). The angle of the stifle joint would significantly impact the PT and its viscoelastic properties. Studies regarding PT biomechanics and viscoelastic properties have shown that changes in the stifle flexion angle can significantly impact the PT's tone, stiffness, and elasticity. In humans, it is hypothesized that knee joint position plays a role in determining the elasticity of the PT, representing the highest elasticity at flexion using the elastography method (Berko et al. 2015). Reportedly, flexion angles of 90° resulted in the highest PT tone and stiffness in both dominant and non-dominant legs (Chen et al. 2019). Other studies reported that elastography assessment of the patellar ligament demonstrated a considerably lower percentage of stiffness in the standing position (135°) than in other positions (McCagherty et al. 2020). Even though human and canine knees are not anatomically identical, a prior investigation discovered sufficient biomechanical similarities to justify comparing specific characteristics (Haut et al. 1992; Burgio et al. 2022).

To the best of our knowledge, in live animals (not cadavers), no studies have addressed all five parameters included in the Myoton device on dog PT. These parameters include muscular tone, dynamic stiffness, logarithmic decrement, relaxation time, and creep. Therefore, this study aimed to investigate PT biomechanical and viscoelastic properties in response to the effects of muscle relaxants and under different knee loading angles (normal position, flexion, and extension). Analysis of a dog's PT using the Myoton

device could provide reference values on PT biomechanical and viscoelastic properties in various circumstances. These findings may offer an objective diagnostic procedure or comparison between the various examination techniques. We hypothesized that the biomechanical and viscoelastic properties of the patellar tendon (PT) in dogs will exhibit significant variations under the influence of the muscle relaxant, particularly in response to changes in stifle joint angles.

1.3. Material and methods

1.3.1. Animals

Five adult female Beagles (B1, B2, B3, B4, and B5) with a mean age of 10.6 ± 0.55 years (range, 10–11 years), mean body weight of 11.4 ± 0.74 kg (range, 10.5–12.2 kg), and body condition score of 3 were used in this study. The dogs were provided by the Yamaguchi University Animal Medical Centre as experimental dogs and had no 1) history of lameness, 2) relationship to any orthopedic examination, and 3) radiographic evidence of joint disease. The protocol was approved by the Committee on the Ethics of Animal Experiments of the Yamaguchi University, Japan (Protocol Number: 539).

1.3.2. Anesthesia and monitoring

Anesthesia was administered to all dogs as it would be easier to manipulate the various stifle angle positions during the examination to create a condition almost identical to those obtained from living dogs. All dogs were fasted for at least 12 hours before receiving anesthesia. The dog's left and right cephalic veins were catheterized using a 22-gauge catheter (Terumo Co., Ltd., Tokyo, Japan) for intravenous infusion of fluids and rocuronium. Ringer's acetate solution (5

mL/kg/hour, Veen F, Fuso Pharmaceutical Industries, Ltd., Osaka, Japan) was administered with a precision infusion pump (TOP-3300; TOP Corporation, Tokyo, Japan).

Induction was started with propofol 1% (Mylan®, Pfizer, Tokyo, Japan) at 7 mg/kg intravenously. An 8 mm endotracheal tube was inserted into the trachea and connected to an anesthetic machine (Dräger Fabius® Plus, Lübeck, Germany) and maintained with isoflurane (Mylan®, Pfizer, Tokyo, Japan) delivered via a 2-liter rebreathing bag. The anesthetic depth was controlled by maintaining isoflurane within 1.5–2.0 minimum alveolar concentration. To ensure the dogs were in stage III plane 3, jaw tone, eye position, pupil size, and several reflexes, including palpebral, swallowing, and pedal reflexes, were assessed. During the experiment, several cardiopulmonary variables that were measured by electrocardiography, pulse oximetry, capnography, temperature, and oscillometric non-invasive blood pressure were monitored using a multiparameter monitor (BSM-6301, Life Scope, Nihon Kohden, Tokyo, Japan) and noted on the anesthetic record every 5 minutes by the anesthetist. The body temperature was maintained between 37.5°C and 38.0°C with a patient warming system (775, 3M™ Bair Hugger™, Maplewood, MN, USA).

1.3.3. Radiographic evaluation

Standard mediolateral radiographs of the stifle joint in the normal, extended, and flexed positions were taken using RADspeed Pro (Shimadzu, Tokyo, Japan). Due to concerns discussed earlier, the standing position will hereafter be described as a normal position when taking radiographic examinations. The angle of the normal (140°) stifle joint position was estimated based on the leg position of a

standing dog. Maximal flexion (34°) and extension (135°) were performed on both legs. The angle measurements were determined using a universal goniometer (Takumed, Sankei Kanko Co., Ltd., Kyoto, Japan).

The main criteria for determining acceptable image results were superimposition of the femoral condyles and fabellae of the gastrocnemius muscle and that the fibular head should be positioned caudally along the proximal section of the tibial condyle. The total PT length (PTL) was determined as specified by a previous study (de Moya and Kim 2020) and was measured from the distal aspect of the patella to the proximal aspect of the tibial tuberosity (Figure 1.1). Additionally, an illustration was provided to highlight the changes in PT shape that occur at different stifle angles (Figure 1.2). The results of PTL on varied stifle angles are demonstrated in Table 1.1. A radiographic reference ball measuring 25 mm was utilized to reduce scaling error during measurement. This examination was performed using SYNAPSE QA (Fujifilm, Tokyo, Japan).

1.3.4. Neuromuscular blockade and monitoring

Before administering muscle relaxant, neuromuscular function was evaluated on a thoracic limb through responses to train-of-four (TOF) stimulation utilizing a muscle relaxation module (AF-201P, Nihon Kohden, Tokyo, Japan) in conjunction with a display monitor (VA-201R, Nihon Kohden, Tokyo, Japan). The dog was positioned in lateral recumbency, and the extended limb was positioned parallel to the table with the antebrachium extended. At the level of the medial epicondyle of the humerus, two needles were implanted subcutaneously across the ulnar nerve and positioned 2 cm apart. Meanwhile, alligator clips (101P-B, K942B, Nihon Kohden, Tokyo, Japan) secured both needles to the TOF muscle relaxation

module. The acceleration transducer (TA-101P, P036A, Nihon Kohden, Tokyo, Japan) was applied to the palmar aspect of the paw using surgical tape (Micropore Surgical Tape, 2.54 cm wide; 3M Health Care, Maplewood, MN, USA), and carpus flexion was elicited. A temperature sensor (TT-101P, P036B, Nihon Kohden, Tokyo, Japan) was inserted into the gingiva of the upper lips.

Stabilization and calibration were performed before the administration of rocuronium (Eslax®, MSD Connect, Rahway, NJ, USA). Signal stabilization was performed using a TOF sequence every 15 seconds (2 Hz, 50 mA) for 10 minutes to facilitate twitch potentiation. Moreover, the monitor's built-in automatic calibration function calibrated the accelerometric measurement. At the beginning of the assessment and baseline, the response remained stable for 5–10 minutes, and a bolus dose of rocuronium (0.5 mg/kg) was administered intravenously. Immediately after, a maintenance dose was administered at 0.2 mg/kg/hr using a precision syringe infusion pump (TOP-5530; TOP Corporation, Tokyo, Japan) The infusion rate was adjusted in increments ranging from 0.2 to 0.5 mg/kg/hour, with at least 2 minutes between each adjustment. The blockade was successful when none of the four twitches could be observed. Infusion was terminated once all measurements were completed. Subsequently, the TOF ratio was monitored until it returned to >90% to ensure that the effects of muscle relaxant had worn off before discontinuing isoflurane administration.

1.3.5. Procedure of assessment

A hand-held MyotonPRO device (MyotonPRO, Myoton Ltd, Tallinn, Estonia) was programmed to perform a series of scans at regular intervals every second, each of which would consist of a short-duration (15 ms) impulse using a

minimum amount of mechanical force (0.4 N) and gentle precompression (0.18 N). Based on the mechanical dynamic response method, it will provide a subsequent computation of parameters characterizing the PT's biomechanical (tissue/muscle tone, dynamic stiffness, and decrement) and viscoelastic properties (mechanical stress relaxation time and ratio of relaxation and deformation time).

The multi-scan measurement consists of five individual measurements (the instrument generated five rapid mechanical impulses) and is automatically reported as the average of these observations. Multi-scan measurements were conducted five times for the three different stifle angles on both legs and groups. Following this, analysis was performed using the average of the five repetitions. All dogs were positioned in lateral recumbency, and all measurements were performed by a single examiner (DA). Moreover, to prevent misinterpretation due to the stability factor, the leg that rested on the examination table was utilized as the standard for measuring.

The same dog was subjected to two experimental procedures. All dogs were evaluated prior to rocuronium administration; this group is the control group. After completing all evaluations, rocuronium was delivered to the same dog, after which they represented the muscle relaxation group and underwent evaluations similar to those previously mentioned. The overlying hair on both patellar ligaments was clipped to avoid any potential bias. The PT was determined by determining the midpoint of the distance between the distal pole of the patella and the tibial tuberosity according to each stifle joint position angle. A standard probe (3 mm) was directed to the designated area and measured the PT by lightly applying the contact detection sensor perpendicularly to the measurement surface. The measurements were repeated when the coefficient of variation was >3%.

Nevertheless, the results were retained in every other circumstance. The mean data were used for statistical analysis.

1.3.6. Parameters

The Myoton device provides five distinct indicators to ensure accurate and reliable outcomes, including tone/oscillation/frequency (Hz, Hertz), stiffness (N/m, Newton/meter), decrement/elasticity (log, logarithmic decrement), relaxation time (ms), and creep (Deborah number [dn]). Tone signifies the tension when a tissue remains passive at rest or without voluntary contraction. The stiffness value is computed as the maximal oscillation acceleration and tissue deformation sensed by the transducer. The ability of soft tissues to return to their original shape after being deformed is referred to as elasticity. Furthermore, elasticity can be considered the inverse of tissue oscillational dampening (the larger the decrement, the lower the elasticity). Relaxation time is defined as the time required for the tissue to recover after being displaced. Creep denotes the constant lengthening of tissue in response to repeated tensile stress (ratio of relaxation and deformation time).

1.3.7. Statistical analysis

Mean values and standard deviation (SD) were used to explain the information acquired from the assessment. Two-way analysis of variance (ANOVA) with repeated measures ANOVA (RM ANOVA) was used to analyze the effect of treatments (control and muscle relaxation) and stifle angles (normal position, extension, and flexion) on the changes in the biomechanical (tone, stiffness, and decrement) and viscoelastic (relaxation time and creep) characteristics of the PT. The Shapiro–Wilk test was used to determine the normal

data distribution. The interaction effect between different stifle angles and the effects of muscle relaxants on the biomechanical and viscoelastic characteristics of the PT was analyzed with the same method. Bonferroni test was performed for post hoc comparisons. Mauchly's test of sphericity was used to evaluate the variances of the differences between all combinations of the related groups (analysis of sphericity). The Greenhouse–Geisser assumption was performed to analyze the interaction when sphericity was violated. Pearson correlation analysis was used to observe the relationship between dog body weight and PT length. SPSS version 27 (IBM SPSS Statistics, version 27, SPSS Inc, Chicago, IL, USA) was used for all analyses. Differences were significant at $P < 0,05$.

1.4. Results

Table 1.2 shows the descriptive statistics for PT parameters contributing to its biomechanical and viscoelastic properties.

1.4.1. Tone

PT tone values are displayed in Figure 1.3. Two-way RM ANOVA revealed significant interactions between treatment and position ($F [1.4, 34] = 17.987$; $P < 0.001$). The effects of different treatments (control and muscle relaxation) on PT tone depended on stifle angle position. In the normal position, PT tone was significantly higher in the control group (22.99 ± 0.99 Hz) than in the muscle relaxation group (18.81 ± 0.44 Hz) ($F [1,24] = 372.825$; $P < 0.001$), with a mean difference of 4.18 Hz (95% CI [3.73, 4.62]). In the extended position, PT tone was significantly higher in the control group (27.66 ± 0.55 Hz) than in the muscle relaxation group (24.67 ± 0.54 Hz) ($F [1,24] = 2,361.062$; $P < 0.001$), with a mean

difference of 2.99 Hz; (95% CI [2.86, 3.11]). In the flexed position, PT tone was also significantly higher in the control group (31.61 ± 0.46 Hz) than in the muscle relaxation group (27.68 ± 0.53 Hz) (F [1,24] = 1,486.196; P < 0.001), with a mean difference of 3.93 Hz (95% CI [3.72, 4.14]).

The effect of stifle angle position on PT tone value varied depending on the treatment. In the control group, PT tone was lower in the normal position (22.99 ± 0.99 Hz) than in the extended position (27.66 ± 0.55 Hz), with a mean difference of 4.67 Hz (95% CI [4.13, 5.21]). However, PT tone was higher in the flexed position (31.61 ± 0.46 Hz) than in the normal and extended positions, with a mean difference of 8.62 Hz (95% CI [8.04, 9.21]) and 3.95 Hz (95% CI [3.68, 4.22]), respectively (F [1.3,31] = 1,050.686; all P < 0.001). Similarly, in the muscle relaxation group, PT tone was lower in the normal position (18.81 ± 0.44 Hz) than in the extended position (24.67± 0.54 Hz), with a mean difference of 5.86 Hz (95% CI [5.68, 6.03]). PT tone was higher in the flexed position (27.68 ± 0.53 Hz) than in the normal and extended positions, with a mean difference of 8.87 Hz (95% CI [8.68, 9.05]) and 3.01 Hz (95% CI [2.79, 3.22]), respectively (F [2,48] = 7,231.708; all P < 0.001).

1.4.2. Stiffness

The difference in stiffness between the control and muscle relaxation groups in various positions and at different stifle angles is illustrated in Figure 1.4. Two-way RM ANOVA revealed significant interactions between treatment and position (F [2, 48] = 2,2295.392; P < 0.001). Notably, the effects of treatment on PT stiffness depended on the stifle angle position. In the normal position, PT stiffness was significantly higher in the control group (481 ± 4.28 N/m) than in the muscle

relaxation group (456 ± 2.01 N/m) (F [1,24] = 1,206.193; P < 0.001), with a mean difference of 25 N/m (95% CI [23.77, 26.78]). Similarly, in the flexed position, PT stiffness was significantly higher in the control group (745 ± 1.64 N/m) than in the muscle relaxation group (635 ± 1.79 N/m) (F [1,24] = 70,860.065; P < 0.001), with a mean difference of 110 N/m (95% CI [109, 111]). In the flexed position, PT stiffness was also significantly higher in the control group (943 ± 1.40 N/m) than in the muscle relaxation group (765 ± 1.34 N/m) (F [1,24] = 16,1471.953; P < 0.001), with a mean difference of 178 N/m (95% CI [176, 178]).

The interaction also indicated that the effect of stifle angle position on PT stiffness varied depending on the treatment. In the control group, PT stiffness was lower in the normal (481 ± 4.28 N/m) than in the extended (745 ± 1.64 N/m) position, with a mean difference of 264 N/m (95% CI [261, 266]). However, PT stiffness was higher in the flexed position (943 ± 1.40 N/m) than in the normal and extended positions, with a mean difference of 462 N/m (95% CI [459, 463]) and 198 N/m (95% CI [196, 198]), respectively (F [1.2,30] = 152,646.443; all P < 0.001). Similarly, in the muscle relaxation group, PT stiffness was lower in the normal (456 ± 2.01 N/m) than in the extended (635 ± 1.79 N/m) position, with a mean difference of 179 N/m (95% CI [177, 180]). PT stiffness was higher in the flexed positions (765 ± 1.34 Hz) than in the normal and extended positions, with a mean difference of 309 N/m (95% CI [307.774, 310.230]) and 130 N/m (95% CI [129, 131]), respectively (F [2,48] = 18,7771.155; all P < 0.001).

1.4.3. Decrement

Two-way RM ANOVA indicated no significant interaction effect (F [2,48] = 2.267; P = 0.115), indicating no combined effect for treatment and position on

decrement as depicted in Figure 1.5. However, both main effects of treatment and position were statistically significant ($P < 0.001$). The main effect of treatment showed a statistically significant difference in decrement between treatments across all positions ($F [1, 24] = 689.039$; $P < 0.001$). Moreover, the main effect of position showed a statistically significant difference in decrement between all positions across all treatments ($F [2, 48] = 4,310.934$; $P < 0.001$).

1.4.4. Relaxation time

Figure 1.6 illustrates the difference in relaxation time between the control and muscle relaxation groups at various stifle angle positions. Two-way RM ANOVA revealed significant interactions between treatment and position ($F [1.3, 31] = 3,428$; $P = 0.04$). The effects of the different treatments on the PT relaxation time depended on the stifle angle position. In the normal position, PT relaxation time was significantly shorter in the control group (10.05 ± 0.38 ms) than in the muscle relaxation group (12.10 ± 0.71 ms) ($F [1,24] = 189.320$; $P < 0.001$), with a mean difference of 2.05 ms (95% CI [1.73, 2.35]). Similarly, in the extended position, PT relaxation time was significantly shorter in the control group (6.38 ± 0.16 ms) than in the muscle relaxation group (8.36 ± 0.62 ms) ($F (1,24) = 184.204$; $P < 0.001$), with a mean difference of 1.98 ms (95% CI [1.67, 2.27]). In the flexed position, PT relaxation time was also significantly shorter in the control group (5.65 ± 0.10 ms) than in the muscle relaxation group (7.30 ± 0.49 ms) ($F [1,24] = 241.977$; $P < 0.001$), with a mean difference of 1.65 ms (95% CI [1.43, 1.86]).

The interaction also indicated that the effect of stifle angle position on PT relaxation time varied depending on the treatment. In the control group, PT relaxation time was longer in the normal (10.05 ± 0.38 ms) than in the extended

(6.38 ± 0.16 ms) position, with a mean difference of 3.67 ms (95% CI [3.52, 3.81]). However, PT relaxation time was shorter in the flexed position (5.65 ± 0.10 ms) than in the normal and extended positions, with a mean difference of 4.4 ms (95% CI [4.24, 4.55]) and 0.73 ms (95% CI [0.65, 0.80]), respectively (F [1.3,32] = 4,242.062; P < 0.001). Similarly, in the muscle relaxation group, PT relaxation time was longer in the normal position (12.10 ± 0.71 ms) than in the extended position (8.36 ± 0.62 ms), with a mean difference of 3.74 ms (95% CI [3.17, 4.31]). Nevertheless, PT relaxation time was shorter in the flexed position (7.30 ± 0.49 ms) than in the normal and extended positions, with a mean difference of 4.8 ms (95% CI [4.46, 5.12]) and 1.06 ms (95% CI [0.69, 1.41]), respectively (F [1.2,31] = 445.094; all P < 0.001).

1.4.5. Creep

Figure 1.7 shows the PT creep values between the control and muscle relaxation groups at various stifle angle positions. Two-way RM ANOVA revealed significant interactions between treatment and position (F [2, 48] = 26.941; P < 0.001). The effects of the different treatments on creep depended on the stifle angle position. In the normal position, PT creep was significantly lower in the control group (0.65 ± 0.01 dn) than in the muscle relaxation group (0.75 ± 0.01 dn) (F [1,24] = 259.251; P < 0.001), with a mean difference of 0.1 dn (95% CI [0.08, 0.10]). Similarly, in the extended position, PT creep was significantly lower in the control group (0.45 ± 0.01 dn) than in the muscle relaxation group (0.51 ± 0.02 dn) (F [1,24] = 137.948; P < 0.001), with a mean difference of 0.06 dn (95% CI [0.05, 0.07]). Furthermore, in the flexed position, PT creep was also significantly lower in the control group (0.40 ± 0.01 dn) than in the muscle relaxation group (0.49 ±

0.03 dn) (F [1,24] = 214.179; P < 0.001), with a mean difference of 0.09 dn (95% CI [0.08, 0.11]).

The interaction also indicated that the effect of stifle angle position on PT creep varied depending on the treatment. In the control group, PT creep was higher in the normal position (0.65 ± 0.01 dn) than in the extended position (0.45 ± 0.01 dn), with a mean difference of 0.2 (95% CI [0.18, 0.21]). However, PT creep was lower in the flexed position (0.40 ± 0.01 dn) than in the normal and extended positions, with a mean difference of 0.25 dn (95% CI [0.24, 0.26]) and 0.05 dn (95% CI [0.04, 0.06]), respectively (F [1.2,30] = 2,260.501; all P < 0.001). Similarly, in the muscle relaxation group, PT creep was higher in the normal position (0.75 ± 0.01 dn) than in the flexed extension (0.51 ± 0.02 dn), with a mean difference of 0.24 dn (95% CI [0.22, 0.24]). Nevertheless, PT creep was lower in the flexed position (0.49 ± 0.03 dn) than in the normal and extended positions, with a mean difference of 0.26 dn (95% CI [0.23, 0.26]) and 0.02 (95% CI [0.01, 0.03]), respectively (F [2, 48] = 1,820.527; all P < 0.001).

1.4.6. Correlations between body weight and PTL

Table 1.3 demonstrates the correlation between body weight and PTL in the normal, extended, and flexed positions.

1.5. Discussion

The current study is the first to quantify PT's biomechanics and viscoelastic properties in living dogs using Myoton devices. The primary findings showed that the position of the stifle angle and the NMBA affected dog PT's biomechanical and viscoelastic qualities. In addition, the relationship between body weight and PTL (Table

1.3) using Pearson's r statistic was not statistically significant. The author believes the lack of statistical significance might have been caused by the limited sample size (N = 5). The research involved six canines of comparable ages, with a particular emphasis on female subjects to reduce potential sources of variation. The author believes that gender and age could influence outcomes, drawing parallels with human medicine. Despite the exclusive focus on female dogs, the study's pioneering methodology and baseline data can form a strong foundation for future research.

The administration of muscle relaxants resulted in a notable reduction in tone, stiffness, and decrement. The authors postulate that muscle relaxant was unlikely to impact tendons directly due to their primer influence on muscle relaxation. Around the stifle joint, the quadriceps femoris and the posterior muscle compartment (plantaris, articulus genu, semitendinosus, semimembranosus, and popliteus) are responsible for joint stabilization and movement. Furthermore, by preventing muscle contraction, the PT experiences less stress and strain, decreasing tone, stiffness, and decrement. The explanation aligns with the reference by (Appiah-Ankam and Hunter 2004; de Cassia Marqueti et al. 2019; Finni et al. 2023; Freedman et al. 2018; Subramanian et al. 2018; Wang et al. 2012), which states that the loading conditions or forces occurring on a tendon are controlled by the surrounding muscles, which attach to the tendon and contract to generate force. Multiple studies have also provided evidence of the efficacy of muscle relaxants in canines undergoing orthopedic surgery (Popovici et al. 2014; Alderson et al. 2007; Dugdale MA et al. 2002; Auer 2007). This highlights its essential role in optimizing muscle relaxation during medical procedures, indirectly affecting tendon function and overall joint stability. The relaxation time and creep were significantly lower in the control group than in the muscle relaxation group. Tissues with higher stiffness might rapidly influence the condition to return to their original shape. A faster relaxation time indicates that the tendon

returns to its initial length more quickly after being stretched. The time-dependent behavior of materials under applied stress or strain, widely observed in biological tissues, is called viscoelasticity. The association between tissue stiffness and viscoelastic qualities has been reported in several studies (Klich et al. 2020; Sasajima et al. 2022; Chaudhuri et al. 2020; Lange and Fabry 2013). Tissues with higher stiffness tend to have slower relaxation rates and creep under constant stress or load. The observed disparities in relaxation times and creep values between the groups indicate the complex viscoelastic nature inherent to these biological components, underscoring the broader implications of tissue mechanics within physiological contexts.

The evaluation of PT tone in various positions revealed notable differences within the control and muscle relaxation groups. Our studies indicated that PT tone was the lowest at normal position and the shape was not straight or elongated (Figure 1.2). The absence of elongation suggests a state of rest, corroborated by the lower tension observed. This aligns with the findings of another study (McCagherty et al. 2020), where dogs displayed minimal PT tension while standing, emphasizing how their natural posture fosters relaxation in their physiological state. The highest value was observed in the flexion for both groups. This observation can be attributed to the mechanics of knee flexion, wherein the patella is displaced away from the femur, facilitating the lengthening and stretching of the tendon. Notably, PT elongation is shown in flexion and extension positions (Table 1.1). However, it was exclusively during knee flexion that the PT tone displayed its peak value. The phenomenon might be attributed to the heightened stress experienced by the PT in the flexed position compared to the other positions. In line with this notion, previous research (Kuervers et al. 2021; Hardy et al. 2017; Pearson et al. 2017) using elastography reported that PT exhibits more significant shear strain and stiffness during flexion, reflecting higher passive tension generated by the surrounding musculoskeletal structures. Indeed, a study

by (Chen et al. 2019) using a Myoton device showed that PT tone at 90° (flexion) was the highest compared to that at 0°, 30°, and 60° degrees.

The stiffness results in the flexion position were the highest in both the control and the muscle relaxation groups across all positions. Similar to the tone parameter, the PT experienced the highest stiffness in the flexed position due to the tendon being stretched (Figure 1.2). These results are in accordance with (Okamura et al. 2015), which states that the gastrocnemius muscles become stiff due to a greater dorsiflexion angle during static stretching. Another study (Schneebeli et al. 2020) showed that AT measurements taken with the foot in 0° of dorsiflexion significantly increased stiffness compared to those obtained when the subject was standing or in a relaxed position (hanging freely over the edge of the examination bed). Given the more linear explanation, the measurements in this research were taken at the PT's midpoint, which was subjected to the highest stress. This argument is consistent with previous observations, which reported that tendon stress would be higher at the middle of the PT (roughly 50% of the length), approximately 20–25 mm from the patella's apex (Kongsgaard et al. 2007). Other investigations also found that the structure of the PT and subcutaneous fat, which generate PT strain when the knee is flexed, is strongly associated with the higher stiffness values of the PT as the knee angle increases (Chen et al. 2019). Research using elastography has confirmed that the relative stiffness for both the PT and quadriceps muscles increases as the knee approaches its maximum flexion angle (Wadugodapitiya et al. 2021).

Regardless of the position, the most significant decrement values were found in the flexion position for both groups. Decrement parameters from the Myoton device were used to inversely describe elasticity, suggesting that as the value of decrement increases, the elasticity of the tissue decreases. As shown in Table 1.2, a similar pattern was seen in the current study. The association can be highlighted by the fact that when the tissue becomes

stiff, its ability to deform and return to its normal shape decreases. Stiffness and elasticity are typically inversely related in biological tissues, including tendons and cartilage. These tissues comprise a dense network of fibers or proteoglycans that resist deformation (Bohm et al. 2015). When subjected to strain or stretch, tendon fibers become denser and less flexible. These alterations impair the tendons' ability to deform when a force is applied and their capacity to stretch and recover, leading to a loss of elasticity (de Cassia Marqueti et al. 2019). In other words, increased stiffness in biological tissue is often accompanied by a decrease in elasticity as the tissue becomes less able to deform under load and dissipate energy. The findings are congruent with (Ramazanoglu et al. 2021) on the masseter muscle and (Agyapong-Badu et al. 2016) on the rectus femoris and biceps brachii. Their results revealed that the elasticity decreases as the tone and stiffness of muscles increase.

The current study shows that flexion in both groups produced the shortest relaxation time. Conversely, relaxation time was consistently the longest in the normal position for both groups. The essential assumption is that the PT is an example of a biological tissue that exhibits both elasticity and viscosity. When force is applied to a tendon, it deforms and stores energy elastically. As strain is prolonged, the tendon becomes viscous, losing energy during deformation and relaxation. This ability would give the PT a shorter relaxation time than other tissues, allowing them to quickly restore their original shape and mechanical properties when subjected to repeated stress. This finding is consistent with previous research demonstrating the relationship between tone/stiffness and relaxation time. The observations revealed that the relaxation time was considerably shorter when the tissue/muscle had a higher tone and stiffness (Klich et al. 2020; Ko et al. 2018; Rosicka et al. 2022; Javier Núñez et al. 2023).

Similar to the relaxation time, creep was the lowest during flexion in both groups. In contrast, creep was the highest in the normal position for both groups. Creep represents the tendency of a material to continue to deform over time when subjected to constant load or stress. The author's perspective was that there was an inverse correlation between stiffness and creep due to the viscoelastic properties of the PT. Earlier research (Thornton et al. 2001) identified a correlation between water and creep on ligament viscoelasticity. This study suggests that decreasing water content in the ligaments would result in a reduced viscoelastic response and creep. Further investigations have indicated that removing water molecules around collagen fibrils alters its microarchitecture and increases tissue stiffness (Masic et al. 2015). The PT experienced the highest stiffness during flexion compared to other positions, i.e., increased stiffness will decrease the amount of water molecules around the collagen fibers. This assumption is aligned with a previous investigation (Lozano et al. 2019) that stated that a stiffer PT would restrict water from entering or remaining within the fibers by limiting the movement of water molecules. This phenomenon is evidenced by squeezing the water molecules out or reducing the space between collagen fibers by a compression mechanism. Additionally, several prior studies have suggested an inverse correlation between creep and tone/stiffness in tissues. As tone and stiffness increase, creep decreases (Thornton et al. 2001; Hingorani et al. 2004; Sopakayang and De Vita 2011).

1.6. Conclusion

The study demonstrates that muscle relaxants and the stifle joint angle may alter the biomechanical and viscoelastic properties of the PT. Analysis of the dog's PT tone, stiffness, decrement, relaxation time, and creep reveal distinct responses to joint angles, particularly heightened tone and stiffness with reduced elasticity during flexion. Thus, it enhances our

comprehension of tissue biomechanics by emphasizing interconnected mechanical parameters, particularly in veterinary medicine.

1.7. Table chapter I

Table 1.1. Patellar tendon length (PTL) during various stifle joint conditions.

Position	Patellar length (mm)				
	B1	**B2**	**B3**	**B4**	**B5**
Normal	27.1	28.0	28.1	23.8	24.5
Extension	30.0	30.6	32.8	27.8	27.4
Flexion	28.8	29.5	31.7	26.9	26.4

Abbreviations: mm (millimeters).

Table 1.2. Descriptive statistics for the biomechanical and viscoelastic characteristics of the patellar tendon.

Variable		Control			Muscle relaxation		
		Normal	Extension	Flexion	Normal	Extension	Flexion
Tone (Hz)	Mean	22.99[e]	27.66[a,e]	31.61[a,b,e]	18.81	24.67[c]	27.68[c,d]
	SD	0.99	0.55	0.46	0.44	0.54	0.53
	Range	3.70	2.07	1.71	1.70	2.08	2.02
	95% CI	22.58–23.40	27.43–27.89	31.42–31.80	18.62–18.99	24.44-24.89	27.45-27.90
Stiffness (N/m)	Mean	481[e]	745[a,e]	943[a,b,e]	456	635[c]	765[c,d]
	SD	4.28	1.64	1.40	2.01	1.79	1.34
	Range	16.37	6.22	5.31	7.15	6.30	5.79
	95% CI	480–483	745–746	942–944	455–457	634-636	765-766
Decrement (log)	Mean	0.63[e]	0.78[a,e]	1.46[a,b,e]	0.49	0.63[c]	1.28[c,d]
	SD	0.04	0.07	0.03	0.04	0.04	0.02
	Range	0.18	0.26	0.13	0.17	0.16	0.09
	95% CI	0.61–0.65	0.75–0.82	1.44–1.47	0.47–0.51	0.61-0.65	1.27-1.29
Relaxation time (ms)	Mean	10.05[e]	6.38[a,e]	5.65[a,b,e]	12.10	8.36[c]	7.30[c,d]

	SD	0.38	0.16	0.10	0.71	0.62	0.49
	Range	1.35	0.61	0.39	2.69	2.36	1.80
	95% CI	9.89–10.2	6.31–6.45	5.61–5.70	11.80–12.39	8.10-8.61	7.10-7.51
Creep (dn)	Mean	0.65[e]	0.45[a,e]	0.40[a,b,e]	0.75	0.51[c]	0.49[c,d]
	SD	0.01	0.01	0.01	0.75	0.51	0.49
	Range	0.06	0.07	0.02	0.07	0.08	0.12
	95% CI	0.64–0.66	0.44–0.46	0.39–0.40	0.74–0.75	0.51-0.52	0.48-0.51

Abbreviations: CI, confidence intervals; SD, standard deviation; Hz: Hertz; N/m: Newton/meter; log: logarithmic; ms: milliseconds; dn: Deborah number.

[a]Significantly ($P < 0.05$) different from the value obtained in normal position (control group).

[b]Significantly ($P < 0.05$) different from the value obtained in the extension position (control group).

[c]Significantly ($P < 0.05$) different from the value obtained in normal position (muscle relaxation group).

[d]Significantly ($P < 0.05$) different from the value obtained in the extension position (muscle relaxation group).

[e]Significantly ($P < 0.05$) different from the value obtained in other treatments.

Table 1.3. Correlation between body weight and patellar tendon length.

		1	2	3	4
1.	Body weight				
2.	Normal	0.84			
3.	Extension	0.83	0.91*		
4.	Flexion	0.81	0.90*	0.99**	

* $p < 0.05$, ** $p < 0.01$

1.8. Figures

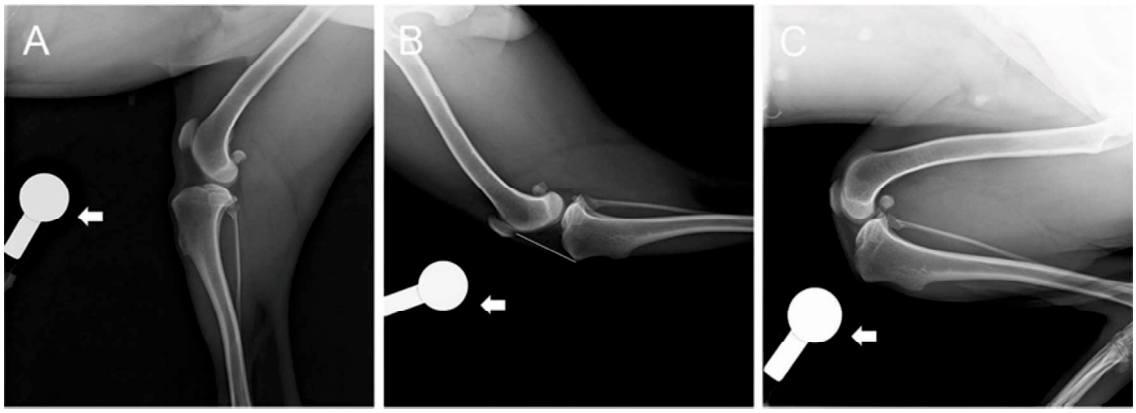

Figure 1.1. Radiographic comparison of the patellar tendon. (A) normal, (B) extended, and (C) flexed positions. Patellar tendon length (PTL) and radiographic reference ball are shown as white lines and arrows, respectively.

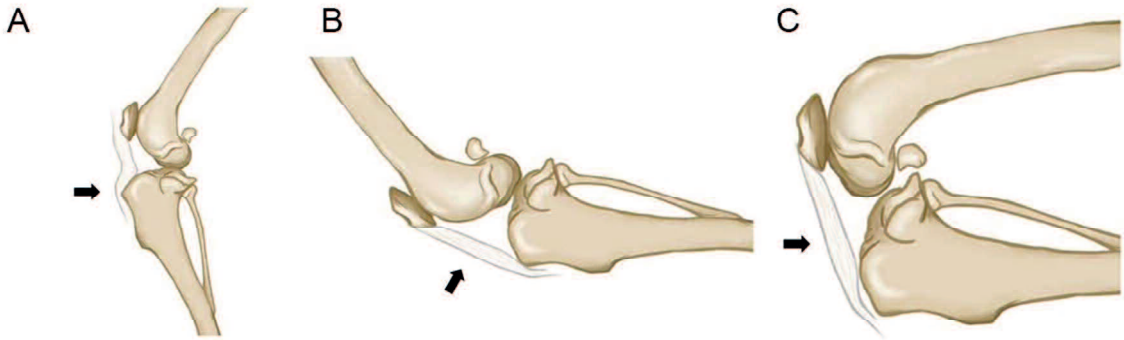

Figure 1.2. Illustration of the patellar tendon shape (arrow). (A) Normal, (B) extension, and (C) flexion of the stifle joint.

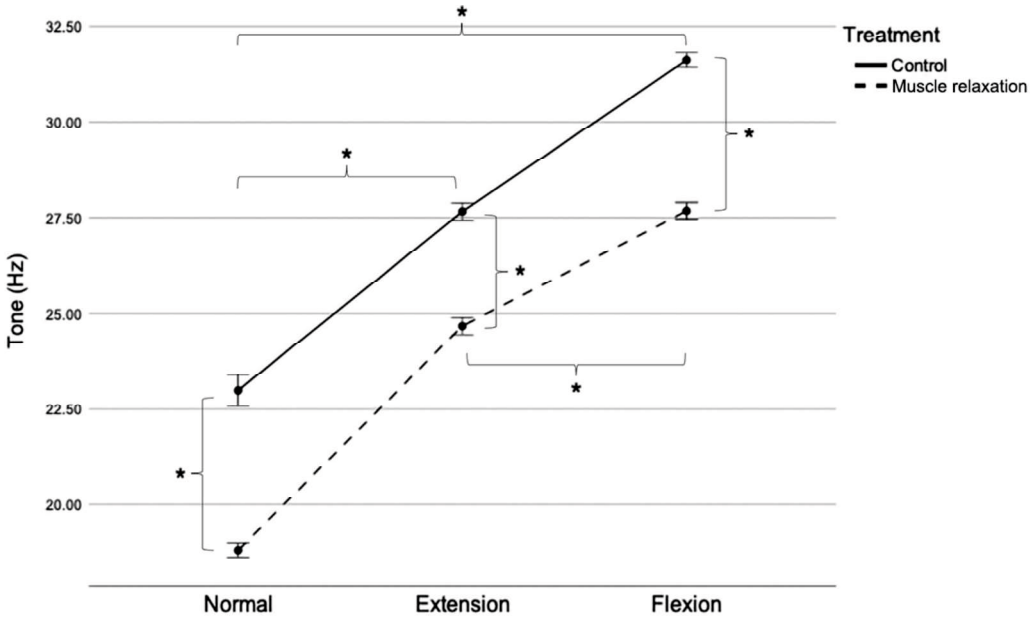

Figure 1.3. Patellar tendon tone in the control and muscle relaxation groups. Mean with SEM. *P < 0.05. Hz, Hertz; SEM, standard error of the mean.

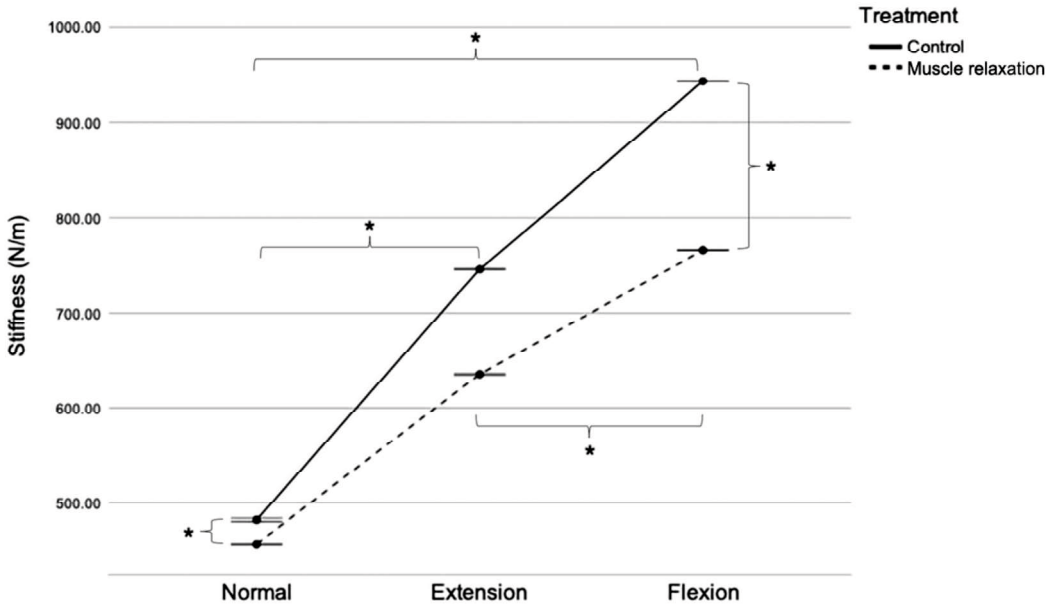

Figure 1.4. Patellar tendon stiffness in the control and muscle relaxation groups. Mean with SEM. *P < 0.05. N/m, Newton/meter; SEM, standard error of the mean.

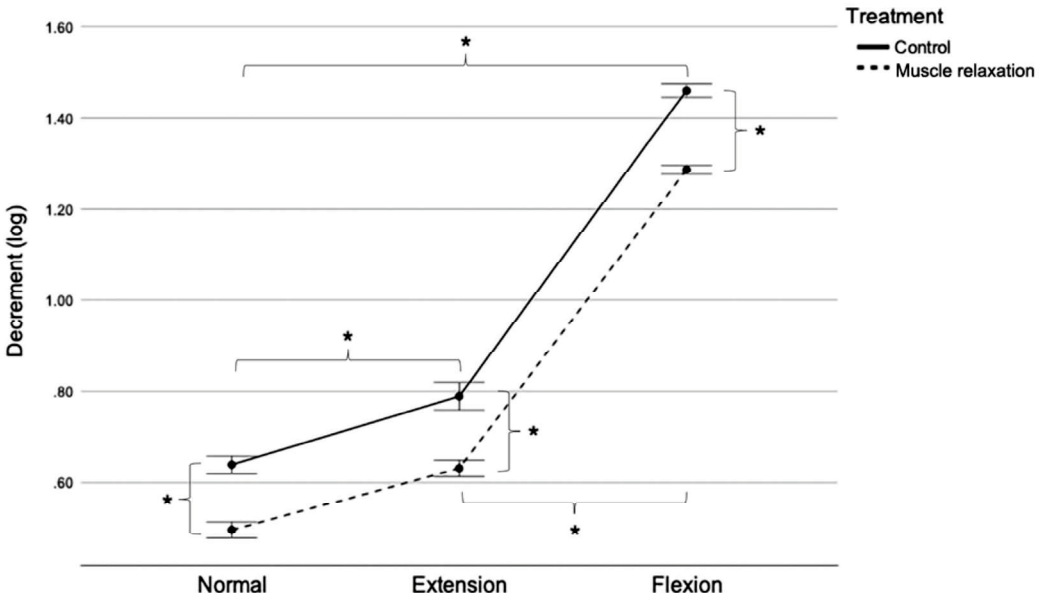

Figure 1.5. Patellar tendon decrement in the control and muscle relaxation groups. Mean with SEM. *P < 0.05. log, logarithmic; SEM, standard error of the mean.

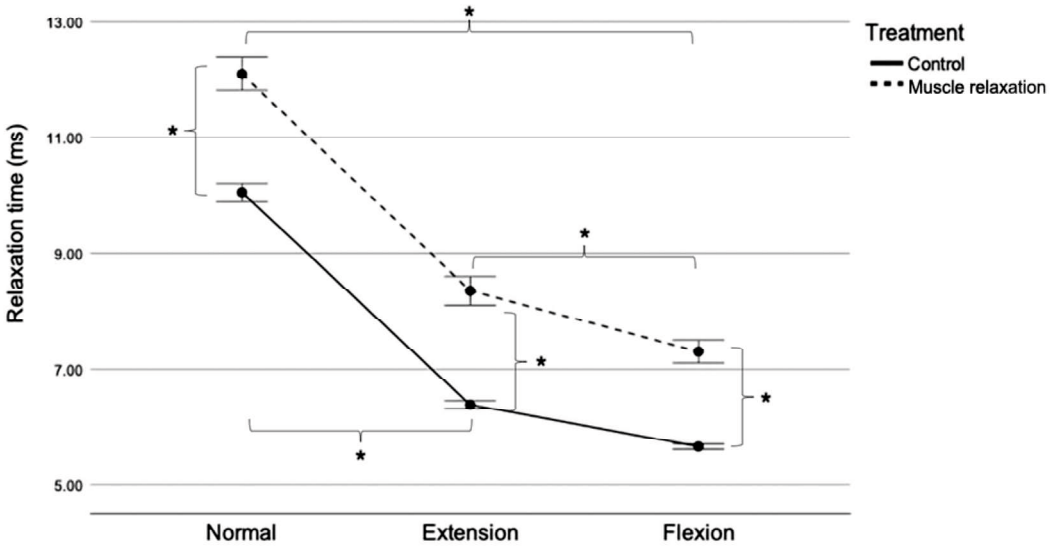

Figure 1.6. Patellar tendon relaxation time in the control and muscle relaxation groups. Mean with SEM. *P < 0.05. ms, milliseconds; SEM, standard error of the mean.

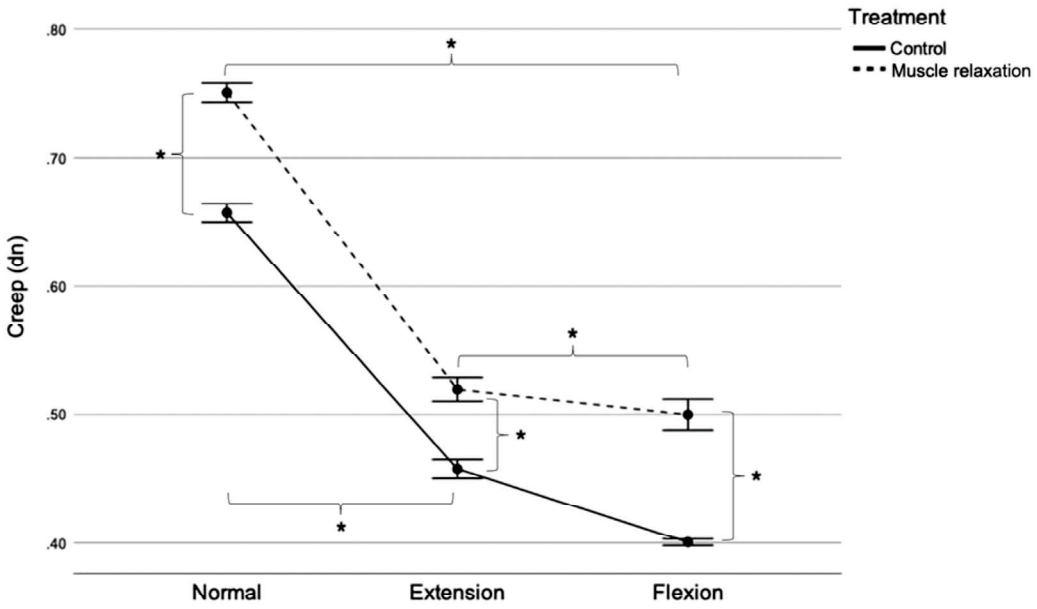

Figure 1.7. Patellar tendon creep in the control and muscle relaxation groups. Mean with SEM. *P < 0.05. dn, Deborah number; SEM, standard error of the mean.

CHAPTER II

Elucidation of the radius and ulna fracture mechanisms in toy poodle dogs using finite element analysis

This work has been published as follows:

Anggoro, D, Purba, M.S., Fei, Jiang., Nishida, N., Itoh, H., Itamoto, K., Nemoto, Y., Munekazu, N., Sunahara, H., and Tani, K. (2024). Elucidation of the radius and ulna fracture mechanisms in toy breed dogs using finite element analysis. *The Journal of Veterinary Medical Science*, 86(5): 575-583. https://doi.org/10.1292/jvms.23-0520. PMID: 38556325.

2.1. Abstract

Fractures occurring in the distal radius and ulna of toy breed dogs pose distinctive challenges for veterinary practitioners, requiring specialized treatment approaches primarily based on anatomical features. Finite Element Analysis (FEA) was applied to conduct numerical experiments to determine stress distribution across the bone. This methodology offers an alternative substitute for directly investigating these phenomena in living dog experiments, which could present ethical obstacles. A three-dimensional bone model of the metacarpal, carpal, radius, ulna, and humerus was reconstructed from Computed Tomography (CT) images of the toy poodle and dachshund forelimb. The model was designed to simulate the jumping and landing conditions from a vertical distance of 40 cm to the ground within a limited timeframe. The investigation revealed considerable variations in stress distribution patterns between the radius and ulna of toy poodles and dachshunds, indicating notably elevated stress levels in toy poodles compared to dachshunds. In static and dynamic stress analyses, toy poodles exhibit peak stress levels at the distal radius and ulna. The Von Mises stresses for toy poodles reach 90.07 MPa (static) and 1090.75 MPa (dynamic) at the radius and 1677.97 MPa (static) and 1047.98 MPa (dynamic) at the ulna. Conversely, dachshunds demonstrate lower stress levels for 5.39 MPa (static) and 231.79 MPa (dynamic) at the radius and 390.56 MPa (static) and 513.28 MPa (dynamic) at the ulna. The findings offer valuable insights for modified treatment approaches in managing fractures in toy breed dogs, optimizing care and outcomes.

2.2. Introduction

The small or toy-breed dogs were at a higher risk of experiencing an antebrachial fracture compared to large-breed dogs, especially in the distal radius and ulna (Boudrieau

R.J. 2003; McCartney et al. 2010; Yu et al. 2010). Fractures in those breeds often result from specific situations, with the most common causes being falls from considerable heights (Bell et al. 2022). These situations include instances where the dog falls out of a caregiver's hand while being carried or when they attempt to jump from a sofa or staircase. Based on the anatomical aspect of the forelimbs, small breed dogs have different lengths and diameter sizes compared to large breed dogs. During weight-bearing activities such as standing, walking, and trotting, the forelimbs of most dog breeds support approximately 60% of the dog's body weight (Lee et al. 1999). In addition, it can be observed that upon landing from a jump, dogs depend entirely on their forelimbs to support their body weight in conjunction with the gravitational forces acting upon them (Zink and Schlehr 2020). Consequently, while dogs of different sizes experience a similar fall, the forces acting on their forelimbs should be distributed differently. Some clinical studies, including experimental and numerical studies, have been conducted to elucidate the higher prevalence of fractures and additional challenges during the healing mechanism of radius and ulna bone in small or toy-breed and large-breed dogs (Brianza et al. 2007; Brianza et al. 2006; Yu et al. 2010).

Experimental studies were typically carried out using either a single or a portion of a cadaver's radius and ulna. (Welch et al. 1997) investigated blood circulation in the forelimbs of 12 deceased dogs. The investigations revealed that small-breed dogs have prolonged bone healing time and increased incidence of non-union due to a reduction of microvascular density in the distal diaphysis. In the same studies, (Welch et al. 1997) further claimed that the limited bone surface contact during surgery corresponds to small diaphyseal diameters of the radius and ulna compared to large-breed dogs. Further research (Brianza et al. 2007) showed toy-breed dogs had lower values moments of inertia (MOI), exposing this breed to more significant local stresses and eventual failure at lower peak

loads when similar normalized loading is taken into large-breed dogs. The MOI is essential in determining how resistant a structure is to bending deformation. Higher MOI craniocaudal and mediolateral values indicate higher bone resistance to bending forces in the craniocaudal and mediolateral planes (Mejia et al. 2019). However, the cadaver test is prohibitively expensive due to the limited number of specimens that can be obtained, making it difficult to carry out many experiments considering different boundary conditions. Moreover, it is challenging to ascertain the distribution of stress and strain at the distal radius, which is thought to be connected to variations in the fracture pattern (Johnson and Troy 2017; Zapata et al. 2017).

In contrast to experimental studies, numerical bone studies, especially in veterinary medicine, were in limited quantities. However, Finite Element Analysis (FEA) has been widely applied and provided valuable insights into explaining distal radius ulna fractures in humans (Edwards and Troy 2012; Johnson and Troy 2017; Pramudita et al. 2022; Revel et al. 2020; Yamazaki et al. 2021). The introduction of FEA has demonstrated enormous potential in resolving various biomedical engineering issues. In the context of veterinary orthopedics, FEA offers a valuable tool that facilitates the prediction and comprehensive understanding of various aspects of bone mechanics. It has enabled researchers to replicate and evaluate the response of bones to diverse loading scenarios. Implementing a simulation-based methodology offers a virtual platform for examining the mechanical reaction of bones, including displacement, stress, and strain distributions along the entire bone and at any location within its cross-section (Oftadeh et al. 2015; Ruffoni and Van Lenthe 2017). The technique provides a viable alternative to studying these phenomena directly in live animals, which may pose ethical or practical challenges.

To the best of our knowledge, no studies have investigated fracture mechanisms in toy breed dogs, especially in toy poodles, by utilizing FEA. The study aimed to investigate

the fracture mechanism of toy poodles by elucidating the stress distribution in the distal radius and ulna during falls. According to the ANICOM study, dachshunds exhibit a lower incidence of forelimb fractures compared to toy poodle (ANICOM 2023). In addition, dachshunds were selected based on their unique skeletal morphology, characterized by an elongated body with short and compact limbs. This conformation provides valuable insights into the role of different skeletal morphologies in fracture patterns. We hypothesized that toy poodles exhibit distinct stress distribution patterns compared to dachshunds, with a concentration of stress observed in the distal region of the radius and ulna.

2.3. Materials and methods

2.3.1. Animals

Four-year-old toy poodle and five-year-old dachshund, weighing 3 kg and 10 kg, participated in the experiment, respectively. The CT data used in this study was obtained from Yamaguchi University Animal Medical Center (YUAMEC) and was initially collected for different purposes. Prior consultation was conducted with the Yamaguchi University Ethics Committee to ensure adherence to animal protection regulations, eliminating the need for additional approval. Thus, the research was not subject to the Animal Research: Reporting of In Vivo Experiments (ARRIVE) regulation. Dogs admitted to the center as regular patients, unrelated to orthopedic issues, had their owners provide informed consent through a signed form before the examination. Subsequently, the data were utilized following anonymization protocols and general consent guidelines.

2.3.2. Anesthesia

Prior to anesthesia, all dogs fasted for a minimum of 12 hr. A 22-gauge catheter (Terumo Co., Ltd., Tokyo, Japan) was used to catheterize the dogs right cephalic veins to administer intravenous fluids. Patients were administered Ringer's acetate solution (5 mL/kg/hr, Veen F, Fuso Pharmaceutical Industries, Ltd., Osaka, Japan) using a precision infusion pump (TOP-3300; TOP Corporation, Tokyo, Japan). The dogs were calm and cooperative, facilitating smooth anesthesia induction without premedication. The induction process was initiated by administering propofol 1% (Mylan®, Pfizer, Tokyo, Japan) at a dosage of 7 mg/kg. The endotracheal tube was inserted into the trachea and connected to an anesthetic machine (Dräger Fabius® Plus, Lübeck, Germany) and maintained with isoflurane (Mylan®, Pfizer, Japan) delivered via a 2-liter rebreathing bag. Throughout the CT scanning, a multiparameter monitor (BSM-6301, Life Scope, Nihon Kohden, Tokyo, Japan) was utilized to measure various cardiopulmonary variables, including electrocardiography, pulse oximetry, capnography, blood pressure, and temperature. The anesthesiologist conducted periodic evaluations at 5 min intervals and documented them in the patient's anesthesia record.

2.3.3. Three-dimensional finite element model

The radius, ulna, humerus, and spongy bone were segmented from a series of 60 slices of CT scan (Supria, Hitachi, Medical Co., Tokyo, Japan) images. The imaging parameters selected included a tube voltage of 120 kV, a tube current of 150 mA, and a slice thickness of 2.5 mm. Based on these structure identifications, a three-dimensional model of the canine forelimb was constructed (Figure 2.1). Following the segmentation, smoothing (canceling the noises), fixing (removing

the wholes), and meshing were performed on the model mentioned above. All these procedures were done using Simpleware ScanIP v21 (Synopsis, Sunnyvale, CA, USA). The finite element models used tetrahedron mesh elements with an averaged 0.2 mm element size. The determination of the element size was based on the convergence results, as the size of the element had been observed to have a correlational effect on the outcomes. The number of nodes and elements for each bone are shown in Table 2.1. The radius and ulna have been categorized into three distinct regions: distal, medial, and proximal. Each specific location's cross-sectional area (CSA) was measured using the same software (Table 2.2).

2.3.4. Bone material property distribution

The bone material is assumed to be homogeneous, isotropic, and linearly elastic (Arias-Moreno et al. 2020; Johnson and Troy 2017; Ruffoni and Van Lenthe 2017; Yamazaki et al. 2021). A comprehensive analysis of high-resolution CT scans determined the differentiation between cortical and cancellous bone. Simpleware ScanIP v21 (Synopsis) was utilized to analyze pictures by applying thresholding and segmentation algorithms to accurately distinguish cortical and cancellous bone based on the Hounsfield Unit (HU) ranges. Threshold values (700–3000 HU for cortex, 100–700 HU for cancellous) were found through refined and repeated testing to reduce noise and artifacts (Nakatsuchi et al. 2006; Hara et al. 2002). Additionally, watershed algorithms improved border delineation, especially in complex or overlapping areas. The subsequent step of visual confirmation involved aligning the segmented regions with observable anatomical structures evident in the CT images, thereby providing additional validation for this model's accuracy and biological significance. The material properties in terms of Young's

modulus and Poisson's ratio were derived from prior research (Hirashima et al. 2021; Lai et al. 2015; Laurent et al. 2020). The humeri of toy poodles and dachshunds share similar mechanical properties, having a Young's modulus of 17,000 MPa and a Poisson's ratio of 0.3. Humeral mass density was determined using the equation $\rho = m/V$, where ρ represents mass density (kg/mm^3), m denotes bone mass (kg), and V signifies bone volume (mm^3). Loads equivalent to half the typical weight of each breed were applied, yielding distinct densities. Toy poodles exhibited a mass density of 4.5×10-4 kg/mm^3, while dachshunds showed a lower density of 1.35×10-4 kg/mm^3. The previous study determined cortical bone mass density as 2.1×10-6 kg/mm^3 and spongy bone as 7.0×10-7 kg/mm^3, with spongy bone exhibiting a significantly lower Young's modulus of 350 MPa while maintaining the same Poisson ratio (Semb, 1966)

2.3.5. Ligament replication

Ligaments (Fig. 1) were constructed with spring elements that produce force only in stretching deformation situations. This approach replicates the ligamentous structures that establish joint connections and prevents bone separation and dislocation. The accumulation of stress on the ulna and carpal bones, caused by the transmission of force from the humerus, ultimately leads to the development of dislocation-like abnormalities. Concerning this condition, the Multi-Point Constraint (MPC) function was implemented at two locations between the ulna-carpal and ulna-humerus bones. The MPC (Figure 2.1) equalizes displacements at the previously mentioned two-bone association, which helps prevent dislocation while maintaining the rotation ability of the joint (Freeman 2022; Martin et al. 2015).

2.3.6. Analysis condition

The boundary conditions were established through the software MSC Patran v21 (Hexagon, Newport Beach, CA, USA), followed by MSC Marc Mentat v21 (Hexagon) to conduct the analysis. The present study utilized two distinct analytical approaches, static and dynamic. The static analysis examines the behavior of bones when subjected to constant load, providing insights into their responses to consistent forces. The dynamic analysis quantified the impacts of rapid shifts in load, simulating scenarios in which dogs experienced falls to the floor. In the context of static analysis, a series of forces (10 N, 20 N, 30 N, 40 N, and 50 N for toy poodles; 30 N, 60 N, 90 N, 120 N, and 150 N for dachshunds) were applied along the Z-axis from the proximal aspect of both the radius and ulna, with the distal portion of these bones fixed. The Z-axis represents a line extending from the distal to proximal aspects of the radius and ulna. The selection of force magnitudes was determined by a ratio based on the body weight difference between toy poodles and dachshunds, resulting in a threefold increase in force for dachshunds. The present study addressed the radius and ulna's mechanical responses and load-bearing capacities at varying force magnitudes, offering valuable insights into the structural behavior of these bones across different dog breeds.

The dynamic analysis was performed with initial velocities of 2800 mm/s and applied to the humerus. The initial velocities for the experiment were determined through a prior investigation involving drop heights of 20 cm, 40 cm, and 80 cm. Among the drop heights tested, 40 cm emerged as the parameter exhibiting the most substantial and relevant differences in fracture mechanisms for toy breed dogs. The decision reflects a commitment to replicating clinical

conditions encountered by these dogs, optimizing experimental resources for efficiency, and ensuring a balanced approach that combines clinical relevance with practical feasibility. This efficient approach facilitated a focused and considerable examination of mechanical dynamics. Under the assumption that the grounding component remains stationary at the moment of impact, the carpal and metacarpal bones were arranged to be fully immobilized across all conditions. Our studies replicate the force dynamics during the landing event within a limited timeframe. The analysis duration of 0.0025 sec was partitioned into 800 segments and the change was observed for each frame. The designated time frame is predicated on the assumption that the fracture occurs approximately simultaneously with the landing. We collected the data at 0.001, 0.0015, 0.002, and 0.0025 sec of the dynamic analysis for further investigation. The Equivalent Von Mises stress and shear stress distributions were automatically calculated using MSC Marc Mentat v21 (Hexagon) software for static and dynamic analysis to elucidate the mechanical factors influencing distal radius fractures.

2.4. Results

2.4.1. Static analysis of radius and ulna

The Von Mises stress (Table 2.3 and Figure 2.2) analysis on the radius and ulna of toy poodles and dachshunds radius and ulna under increasing axial loading, a consistent trend emerges with stress levels escalating from proximal to distal regions. For toy poodles, distal radius stress increases from 16.45 MPa at 10N to 90.07 MPa at 50N, along with a parallel rise in the medial region from 6.86 MPa to 44.83 MPa, and proximal stress increases from 1.18 MPa to 11.65 MPa. Meanwhile, the dachshund's radius stress rose from 1.04 MPa at 30N to 5.39 MPa

at 150N, medial stress from 3.95 MPa to 20.62 MPa, and proximal stress from 0.92 MPa to 4.66 MPa. Shifting the focus to the ulna, toy poodles experience significant increases in distal stress (from 219.95 MPa to 1677.97 MPa), medial stress (from 186.25 MPa to 1001.54 MPa), and proximal stress (from 34.91 MPa to 122.83 MPa). On the other hand, dachshunds demonstrate an increase in distal ulna stress from 48.61 MPa to 390.56 MPa, middle stress from 10.00 MPa to 74.67 MPa, and proximal stress from 1.19 MPa to 10.35 MPa across the 30-150N force range.

The shear global stress (Table 3 and Fig. 2) analysis of the radius and ulna in toy poodles and dachshunds demonstrated a consistent upward trend with increasing loading forces ranging from 10N to 50N. Notably, the distal segments exhibited the most significant stress escalation, while the proximal regions consistently displayed lower stress levels. Specifically, in toy poodles, the shear global stress in the distal radius increased from 0.96 MPa to 7.55 MPa across the force range. The medial segment initiated at 0.11 MPa and a peak at 2.11 MPa, while the proximal region exhibited stress levels ranging from 0.02 MPa to 0.27 MPa. In dachshunds, the distal radius shear global stress rose from 0.25 MPa at 30N to 1.28 MPa at 150N, and the medial stress increased from 0.15 MPa to 0.90 MPa, with proximal stress ranging from 0.007 MPa to 0.06 MPa. Turning to the ulna, toy poodles displayed a significant increase in distal shear global stress, rising from 17.78 MPa to 818.04 MPa, and a notable increase in medial stress from 45.11 MPa to 345.23 MPa. Proximal stresses in toy poodles' ulna increased from 11.37 MPa to 60.34 MPa. In dachshund ulnae, the distal stress increased from 1.83 MPa to 6.09 MPa, medial stress from 0.53 MPa to 4.64 MPa, and proximal stress from 0.54 MPa to 3.33 MPa within the force range of 30-150N.

2.4.2. Dynamic analysis of the radius

The Von Mises stress (Table 2.4 and Figure 2.3) values at the distal region consistently exhibited an escalating trend in stress over time, reaching a peak value of 1090.75 MPa at 0.0025 sec. In contrast, the proximal and medial regions showed lower and more variable stresses, with proximal stresses ranging from 328.35 to 483.25 MPa and medial stresses ranging from 360.85 to 650.32 MPa. Conversely, dachshunds displayed a different pattern. The distal region showed a declining trend in stress, decreasing from 410.55 MPa to 231.79 MPa. The medial and proximal regions of dachshunds exhibited modest peak stresses of 407.21 MPa and 374.65 MPa, respectively.

The shear global stress (Table 2.4 and Figure 2.4) values of toy poodles at the distal and proximal regions displayed a consistent and increasing trend, with peaks at 0.0025 sec, reaching 92.17 MPa and 39.86 MPa, respectively. In contrast, the medial region exhibited a different behavior, with an earlier peak of 57.72 MPa, followed by a subsequent decline. In contrast, dachshunds displayed an increasing shear stress pattern in the distal and medial region, peaking at 55.88 MPa and 44.22 MPa, respectively, at 0.0025 sec. The proximal region in dachshunds exhibited variable stresses over time, reaching a peak of 40.81 MPa at 0.0025 sec.

2.4.3. Dynamic analysis of the ulna

The Von Mises stress (Table 2.4 and Figure 2.3) values consistently increased over time in all three regions (distal, medial, and proximal) for both breeds. The distal ulna of the toy poodle surged significantly from an initial value of 442.86 MPa to a peak of 1047.98 MPa. Similarly, there was a noticeable rise in the medial stress, which accelerated from 518.19 MPa to 841.68 MPa. The

proximal region also experienced increased stress levels, climbing from 327.71 MPa to 617.33 MPa. A similar increasing pattern was observed over time in dachshunds, although the increase was less pronounced compared to toy poodles. The distal stress levels gradually rose from 275.86 MPa to 513.28 MPa. The medial and proximal stress values increased from 371.18 MPa to 549.74 MPa and 217.12 MPa to 341.49 MPa, respectively.

The shear global stress (Table 2.4 and Figure 2.4) values indicate a persistent upward trend across all the regions for both breeds. The distal ulna stress in toy poodles experienced a substantial increase, rising from an initial value of 27.01 MPa to a peak of 78.68 MPa. Likewise, an apparent rise in the medial stress was observed, with a rate of acceleration from 25.23 MPa to 60.17 MPa. The stress levels in the proximal region also demonstrated a notable increase, with an initial value of 39.66 MPa to 66.15 MPa. In contrast, the shear stresses in dachshunds distal, medial, and proximal regions remained comparatively lower, ranging from 19.43 to 63.07 MPa, 15.22 to 55.47 MPa, and 28.56 to 45.41 MPa, respectively.

2.5. Discussion

The assessment of preventive strategies to reduce the incidence of a dog distal radius fracture requires the implementation of non-invasive technologies that can investigate bone strain and fracture resistance at an individual level. Conventional investigation methods such as mechanical testing and observational studies faced limitations due to small sample sizes and ethical concerns. The present studies overcome these restrictions by utilizing FEA, a reliable computational simulation tool with numerous engineering and veterinary medicine applications. Our findings shed light on the mechanical behavior of

radius and ulna bones under loading conditions, contributing to a better understanding of fracture patterns in toy-breed dogs.

The static analysis revealed a consistent trend in stress distribution, with stress levels progressively increasing from proximal to distal regions for both the radius and ulna. Notably, the Von Mises and shear stress levels of the toy poodle's radius and ulna were significantly greater in all regions compared to those of dachshunds. The ulna of the toy poodle displayed an unusual bending condition when exposed to forces ranging from 20 to 50 N, as depicted in Figure 2.2. The phenomenon was investigated using a scalar of 2000 MPa for Von Mises stress and 1000 MPa for shear global stress, seemingly impossible in typical clinical situations. These observed results may stem from the oversimplification of bone geometry in FEA models, potentially failing to capture the complex details of bone structure. Additionally, intentional exaggeration of loading conditions (forces ranging from 20 to 50 N) was employed for investigative purposes. Interestingly, a decrease in stress scalar values, such as the Von Mises stress (Figure 2.5) decrease to 20 MPa for the radius and 200 MPa for the ulna, along with a reduction in shear global stress (Fig. 5) to 10 MPa for the radius and 100 MPa for the ulna, resulted in a similar pattern with higher stress levels in the distal region upon the subsequent application of a 10 N force to the radius and ulna. This stress distribution aligned more closely with clinical conditions. In other words, the static analysis reveals a consistent stress distribution pattern, irrespective of the force applied to the radius and ulna. This persistence suggests the robustness of the observed pattern under varying force conditions. The author's perspective on the current outcomes was that toy poodles and Dachshunds exhibited different body masses, which might be associated with variations in bone stress distribution. Large breed dogs generally have greater total bone mass than smaller breeds, which helps support their weight-bearing ability (Plassais et al. 2017; Rimbault and

Ostrander 2012; Zapata et al. 2022). Bones comprise a solid framework with a dense matrix of collagen fibers and mineralized calcium phosphate crystals, mainly hydroxyapatite. The higher mass of bones corresponds to a more extensive bone material, resulting in enhanced strength and resistance to deformation (Casagrande et al. 2016; Clayton et al. 2009). Toy poodles are characterized by the small size of their skeletal structure, which is naturally adapted to accommodate a smaller body weight. On the other hand, dachshunds are identified by their medium skeletal size to support their wider and elongated body appearance. Studies have indicated that increased body mass is crucial in enhancing bone mechanical performance. When subjected to equivalent forces, bones with greater mass have demonstrated the ability to withstand higher stress levels (Mancuso et al. 2018). The primary reason for this phenomenon is the increased surface area that facilitates the dispersion of applied forces, enhancing the bone's capacity for support. Similar findings were also reported by (Silva et al. 2019; Arias-Moreno et al. 2020), showing that mice subjected to a high-fat diet treatment demonstrated enhanced bone stiffness and strength due to increased body mass.

The analysis of the impact loading on the radius revealed that toy poodles demonstrated consistently higher levels of Von Mises and shear stress across various times. Notably, the heightened stress was evident in the distal region. These findings could be explained by the radius of the toy poodle, which presented with a thinner bone morphology compared to dachshunds. It is essential to acknowledge that geometries such as those observed in long bones frequently utilize beam models within biomechanical assessments, as evidenced by prior research (Arias-Moreno et al. 2020; Chen et al. 2016; Cheong and Bull 2015; Zhang et al. 2018). Based on the beam theory, the resulting stresses depend on the CSA perpendicular to the load when a load is applied axially to a beam. A smaller CSA produces higher stresses for the same applied force (Rajaai et al. 2010; Saffar et al. 2009).

The study found that toy poodles CSA of the radius consistently exhibited reduced dimensions compared to those observed in dachshunds (Table 2), indicating their increased risk of fractures due to higher bone stress levels during loading conditions.

As articulated by (Brianza et al. 2006), the bone structure of toy breed dogs had a CSA position nearer to the centroid, leading to a reduced moment of inertia and heightening the susceptibility to fractures. The author also presumed that the bone density varied in each bone region. Variations in bone density could potentially contribute to observed stress patterns and fracture processes on the bone. The proximal region of the radius is located closer to the humeral joint than the distal region, making it more susceptible to stress and strain (Rao et al. 2014). According to Wolff's law and the concept of mechanotransduction, regions subjected to greater forces and strains demonstrate higher bone density, enhancing their capacity to endure mechanical stresses (Huang and Ogawa 2010; Frost 2003). Conversely, regions that experience lower levels of force exhibit decreased bone density and potentially increased vulnerability to fractures. Several prior investigations have also found that decreased bone density in the distal radius reduces bone resistance to stresses and increases the fracture probability (Casagrande et al. 2016; Clayton et al. 2009; Lill et al. 2003). The analysis of the impact loading on the ulna revealed a consistent increase of both Von Mises and shear stress across all regions, regardless of the breed under consideration. In particular, toy poodles had higher Von Mises and shear stress for each region and time frame, indicating more significant structural deformation during landing. The observed findings can be attributed to the unique anatomical characteristics of the ulna. The ulna is distinguished by its proximal region being more extensive than its distal end, resulting in a distinctive tapering shape. The diminishing width along the bone introduces complex variations in stress distribution across its structure, making stress distribution challenging to manage. Our findings

resonate with (Rao et al. 2014), which states that ulna morphology presents a challenging situation in stress distribution, ultimately giving rise to localized stress patterns within the bone when subjected to external forces. In addition, these outcomes were likely the consequence of variations in the cortical region surrounding the bones. Prior analysis of cortical bone in the dog radius and ulna has been conducted by (Brianza et al. 2006; Brianza et al. 2007; Mejia et al. 2019). The investigations revealed a consistent pattern wherein smaller breeds exhibited thinner cortices and smaller cortical bone regions than larger breeds. A cortical area with a large CSA will effectively distribute shear stresses across a wider surface area, which potentially decreases the peak stresses (Abu-Hammad et al. 2007; Holcombe et al. 2019; Kontulainen et al. 2007; Louis et al. 2010). Thus, the reduced cortical CSA of bones in smaller dog breeds leads to structural differences that make them more susceptible to the effects of impact loading and shear stresses.

The present study acknowledges limitations in replicating the complex biomechanics of the elbow and shoulder joints within a finite element analysis, particularly integrating elements such as cartilage and arthrodesis. Similarly, capturing the nuanced cushioning effects of muscles around the shoulder post-impact or during leg movement in a fall scenario is hindered by the inherent constraints of the model. Simulating clinical scenarios is complicated by the intricate interplay between anatomical features and physiological responses. Careful consideration was given to eliminating these complex factors to ensure the model aligns with the study objectives and produces relevant results. This decision recognizes the necessary compromise between model complexity and practicality.

2.6. Conclusion

the stress distribution patterns analysis in the radius and ulna showed pronounced differences between toy poodles and dachshunds. Toy poodles experienced considerably higher stresses in the examined bones compared to dachshunds. Specifically, the distal regions of the bones showed markedly greater stress values. These findings contribute to understanding the mechanical factors that influence distal radius fractures in toy-breed dogs, establishing the groundwork for implementing targeted preventive measures and improving veterinary care procedures.

2.7. Table chapter II

Table 2.1. Number of elements and nodes of each model.

Model	Element		Nodes	
	Toy poodle	Dachshunds	Toy poodle	Dachshunds
Radius	25133	27808	5559	10069
Ulna	15160	22928	3828	6067
Humerus	41147	43604	7106	9920
Spongy bone	4118	4648	1050	2108

Table 2.2. The cross-sectional area of the radius and ulna (mm^2).

Bone	Toy poodle			Dachshunds		
	Distal	Medial	Proximal	Distal	Medial	Proximal
Radius	17.4	16.24	15.72	57.6	49.71	46.17
Ulna	5.97	10.54	18.37	16.9	42.23	44.12

Table 2.3. Static analysis at multiple locations under varied forces.

Von Mises stress

TP	Force (N)	Locations Distal	Medial	Proximal	DH	Force (N)	Locations Distal	Medial	Proximal
Radius	10	16.45	6.86	1.18	Radius	10	1.04	3.95	0.92
	20	31.99	14.54	2.71		20	2.11	7.99	1.85
	30	54.60	23.21	4.74		30	3.19	12.11	2.78
	40	77.18	33.15	7.53		40	4.28	16.32	3.72
	50	90.07	44.83	11.65		50	5.39	20.62	4.66
Ulna	10	219.95	186.25	34.91	Ulna	10	48.61	10.00	1.19
	20	713.95	563.72	91.45		20	107.54	21.82	2.69
	30	1311.77	912.44	101.37		30	189.31	35.99	4.61
	40	1518.46	977.07	118.79		40	272.09	53.26	7.09
	50	1677.97	1001.54	122.83		50	390.56	74.67	10.35

Shear global stress

TP	Force (N)	Locations Distal	Medial	Proximal	DH	Force (N)	Locations Distal	Medial	Proximal
Radius	10	0.96	0.11	0.02	Radius	10	0.25	0.15	0.007
	20	2.12	0.26	0.06		20	0.50	0.32	0.01
	30	3.54	0.55	0.12		30	0.76	0.50	0.02
	40	5.30	1.11	0.16		40	1.02	0.70	0.04
	50	7.55	2.11	0.27		50	1.28	0.90	0.06
Ulna	10	17.78	45.11	11.37	Ulna	10	1.83	0.53	0.54
	20	158.03	167.81	40.51		20	3.25	0.62	1.17
	30	609.39	238.07	44.81		30	3.33	0.76	1.88
	40	737.82	284.72	54.82		40	3.84	1.49	2.63
	50	818.04	345.23	60.34		50	6.09	4.64	3.33

Data reported in megapascal (MPa); newton (N); toy poodle (TP); dachshunds (DH).

Table 2.4. Dynamic analysis at multiple locations under varied times.

Von Mises stress

TP	Time (sec)	Locations Distal	Medial	Proximal	DH	Time (sec)	Locations Distal	Medial	Proximal
Radius	0.001	452.86	360.85	483.25	Radius	0.001	410.55	290.86	241.22
	0.0015	696.23	583.97	465.48		0.0015	289.26	355.48	255.89
	0.002	825.92	546.26	328.35		0.002	256.83	381.12	257.14
	0.0025	1090.75	650.32	397.17		0.0025	231.79	407.21	374.65
Ulna	0.001	442.86	518.19	327.71	Ulna	0.001	275.86	371.18	217.12
	0.0015	728.25	542.23	478.44		0.0015	361.12	432.61	272.33
	0.002	834.67	697.26	521.28		0.002	437.25	526.12	291.56
	0.0025	1047.98	841.68	617.33		0.0025	513.28	549.74	341.49

Shear global stress

TP	Time (sec)	Locations Distal	Medial	Proximal	DH	Time (sec)	Locations Distal	Medial	Proximal
Radius	0.001	27.89	57.72	30.12	Radius	0.001	18.25	25.27	29.03
	0.0015	36.89	44.05	32.65		0.0015	29.11	29.19	36.12
	0.002	75.15	40.12	35.22		0.002	35.16	35.65	31.77
	0.0025	92.17	37.65	39.86		0.0025	55.88	44.22	40.81
Ulna	0.001	27.01	25.23	39.66	Ulna	0.001	19.43	15.22	28.56
	0.0015	50.22	39.09	42.21		0.0015	34.87	22.19	31.83
	0.002	64.18	48.12	59.07		0.002	38.55	36.04	43.37
	0.0025	78.68	60.17	66.15		0.0025	63.07	55.47	45.41

Data reported in megapascal (MPa); seconds (sec); toy poodle (TP); dachshunds (DH).

2.8. Figure chapter II

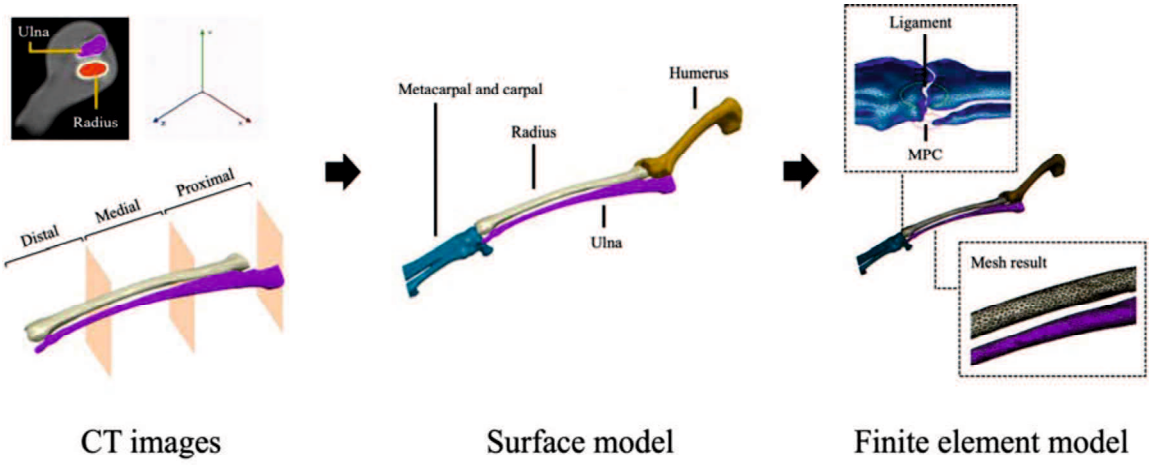

Figure 2.1. Development process for three-dimensional canine forelimb model. Red represent the trabecular region, multi-point constraints (MPC).

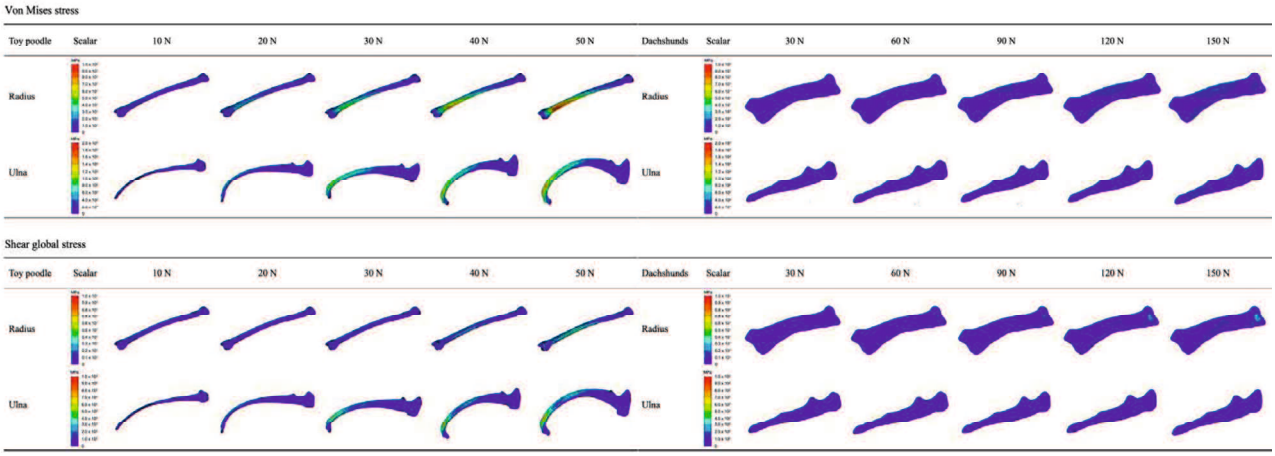

Figure 2.2. The distribution of Von Mises and shear global stress on the radius and ulna under varied force conditions during static analysis. The stress levels are represented by a color scale, with red indicating the highest stress area.

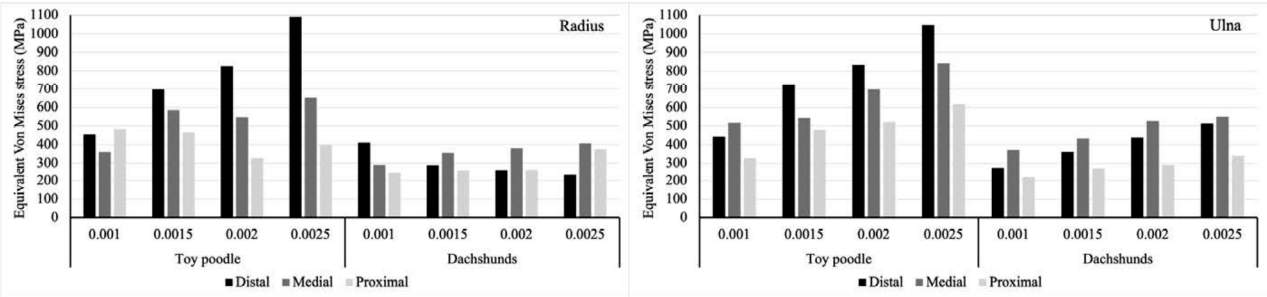

Figure 2.3. Bar graph comparison of Von Mises stress distribution at the radius and ulna on dynamic analysis.

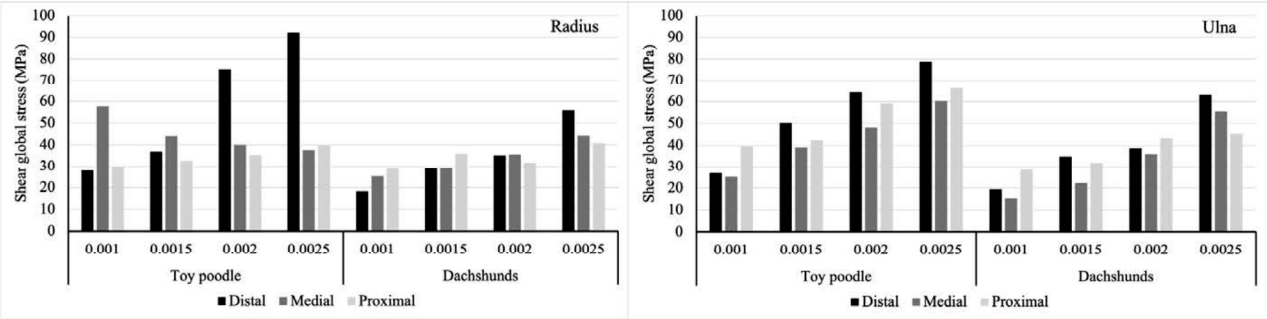

Figure 2.4. Bar graph comparison of shear global stress distribution at the radius and ulna on dynamic analysis.

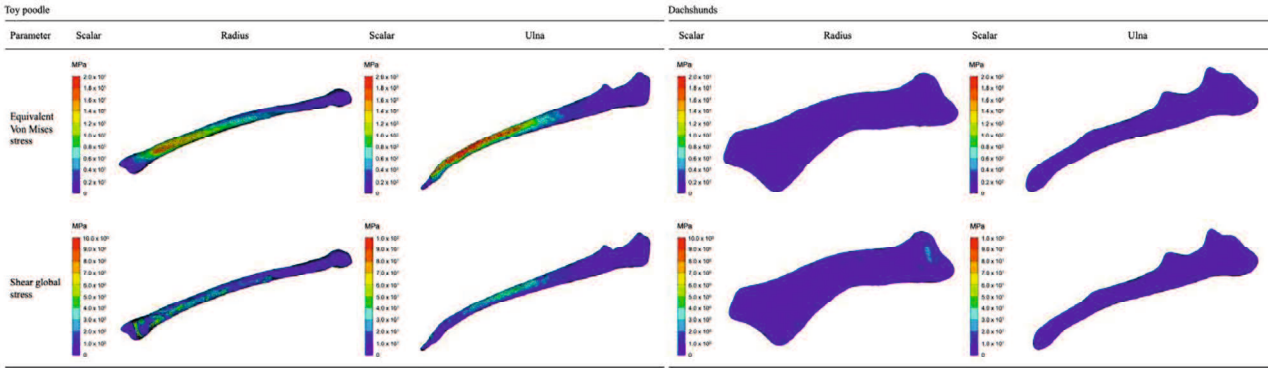

Figure 2.5. Uniform Von Mises and shear global stress distribution in radius and ulna regardless of applied force.

CHAPTER III

Finite element study on post-screw removal stress in toy poodle radius with different plate designs and screw arrangements

This work has been published as follows:

Anggoro, D, Purba, M.S., Fei, Jiang., Nishida, N., Itoh, H., Itamoto, K., Nemoto, Y., Munekazu, N., Sunahara, H., and Tani, K. (2024). Elucidation of the radius and ulna fracture mechanisms in toy breed dogs using finite element analysis. *Open Veterinary Journal*, 14(3):885-894. https://doi.org/10.5455/OVJ.2024.v14.i3.16. PMID: 38682140. PMCID: PMC11052620.

3.1. Abstract

The conducted study provides a comprehensive analysis employing finite element analysis (FEA) to examine stress distribution in the radius of toy poodles after screw removal. The investigation utilized 1.5-mm and 2.0-mm locking compression plates (LCP) with notched head T-Plates, presenting a non-invasive approach to investigate the biomechanical implications of diverse screw hole configurations on bone stress distribution. This research contributes valuable insights that have the potential to refine veterinary orthopedic practices. The study constructed a three-dimensional bone model of the toy poodle forelimb, encompassing the carpal, radius, ulna, and humerus, based on Computed Tomography (CT) images. The simulation design aimed to replicate jumping and landing conditions from a 40 cm vertical distance to the ground, with a specific focus on the immediate consequences of screw removal from the radius bone. The investigation into stress distribution patterns within the two LCPs revealed significant variations. Notably, the radius implanted with the 2.0-mm LCP exhibited a uniform stress distribution compared to the 1.5-mm plates. An interesting finding highlighted localized stress concentration around the screw holes, while the trabecular bone regions displayed lower stress levels in proximity to the screw holes. The study sheds light on the complex dynamics of stress distribution in toy poodle forelimbs post-screw removal, emphasizing the influence of varied plate designs and screw configurations. The observed distinct bone stress distribution patterns provide essential information for veterinarians, offering well-informed insights on clinical decision-making regarding post-screw removal conditions.

3.2. Introduction

Toy breed dogs, especially toy poodles, are admired for their small size and delightful personalities. Nevertheless, the attractive characteristics of these dogs

frequently lead them to engage in activities that could potentially endanger their delicate skeletal structure. These dogs tend to jump and frequently participate in activities that strain their front legs, such as jumping from high places or falling out of a caregiver's hand (Bell et al. 2022). This behavior heightens the risk of fractures and their fragile bone structure, especially in the distal radius and ulna, which are most commonly affected and fractured due to the force of impact (McCartney et al. 2010; Yu et al. 2010). Treating radius fractures in miniature poodle dogs presents a complex clinical situation that requires innovative approaches to ensure effective treatment and optimal post-operative outcomes. The small size, unique bone structure, and limited blood supply of toy poodles are essential features that make it challenging to treat fractures in these dogs (Aikawa et al. 2018; De Arburn Parent et al. 2017). These challenges require veterinarians to carefully analyze and employ specialized techniques to treat them, which could improve the probability of a successful recovery.

Locking compression plates (LCPs) have become a prominent choice in veterinary orthopedics for stabilizing fractures, offering exceptional stability and promoting healing. Previous studies (Alwen et al. 2018; Gibert et al. 2015; Haaland et al. 2009; Kang et al. 2016; Vezzoni et al. 2021) have highlighted the benefits of LCPs, including the flexibility to choose screw types, preservation of critical blood supply, and optimal stability through the use of screws at multiple angles. Despite both 1.5-mm and 2.0-mm LCPs being employed for toy poodle radius fractures, there is a lack of evidence comparing their biomechanical properties. Several complications after the removal of screws have been reported, especially the occurrence of refracture in the radius (Aikawa et al. 2018; De Arburn Parent et al. 2017; Haaland et al. 2009; Vallefuoco et al. 2016). The choice of plate size is a critical decision influencing construction stability and healing. Moreover, the number and placement of screws significantly correlate with screw removal considerations

during post-operative conditions, presenting a risk of refracture. Careful consideration regarding this situation is crucial during the decision-making process for screw removal, highlighting the need for ongoing research to refine fracture management guidelines and enhance long-term outcomes in veterinary orthopedic surgery.

The revolutionary impact of finite element analysis (FEA) in biomedical engineering is evident in its remarkable capabilities to address complex challenges. The methodology is pivotal in predicting biological responses to mechanical stimuli, facilitating efficient analysis of tissue deformation and stress distribution. This procedure has gained extensive traction in human medicine, primarily in elucidating fractures affecting the distal radius ulna (Johnson and Troy 2017; Pramudita et al. 2022; Revel et al. 2020; Yamazaki et al. 2021), its presence in veterinary orthopedics has been relatively limited. However, the evolving potential of FEA in veterinary orthopedics holds promise for addressing a range of complex challenges, offering insights into tissue deformation, stress distribution, and other biomechanical aspects. The interdisciplinary approach highlights FEA's versatility and potential contribution to human and veterinary medicine advancements.

To the best of our knowledge, there have been no studies that addressed the stress distribution on the toy poodle radius after the removal of screws using FEA. The primary objective is to investigate the biomechanical implications of post-operative screw removal in canine radius fractures. We hypothesize that the distribution of stress within the radius exhibits a substantial influence by both plate size and screw hole arrangement. The study employed a non-invasive FEA to investigate the stress distribution within the radius bones of canines as an alternative to experimental cadaveric investigations, addressing the constraints associated with such procedures.

3.3. Materials and methods

3.3.1. Study subject and animal preparation

The experiment involved four-year-old toy poodles with a 3 kg body weight. The dogs were admitted to Yamaguchi University Animal Medical Centre as general patients with no orthopedic issues. The patient was required to fast for a minimum of 12 hours before the anesthetic procedure. An intravenous catheter was inserted into the dog's right cephalic vein using a 22-gauge needle (Terumo Co., Ltd., Tokyo, Japan). Ringer's acetate solution (5 mL/kg/hour, Veen F, Fuso Pharmaceutical Industries, Ltd., Osaka, Japan) was administered using an infusion pump (TOP-3300; TOP Corporation, Tokyo, Japan) throughout the procedure. Anesthesia induction started by administering propofol (Mylan®, Pfizer, Tokyo, Japan) intravenously at a dosage of 7 mg/kg. Following endotracheal intubation, anesthesia was maintained using an anesthetic machine (Dräger Fabius® Plus, Lübeck, Germany) that delivered isoflurane (Mylan®, Pfizer, Tokyo, Japan) through a rebreathing circuit. Continuous physiologic monitoring was accomplished utilizing a multiparameter monitor (BSM-6301, Life Scope, Nihon Kohden, Tokyo, Japan), which recorded electrocardiography, pulse oximetry, capnography, blood pressure, and core temperature readings. Regular anesthetic assessments were conducted at 5-minute intervals, with findings documented by the anesthesiologist in the medical record.

3.3.2. Image acquisition and finite element model construction

The radius, ulna, humerus, and trabecular bone were isolated from 60 CT scan images (Supria, Hitachi, Tokyo, Japan). A comprehensive three-dimensional model of the toy poodle forelimb was successfully constructed based on the

segmentation of skeletal structures, as illustrated in Figure 3.1. Following the completion of segmentation on the model above, the subsequent steps include applying smoothing techniques to reduce noise and address gaps by fixing and meshing the model. In order to streamline the simulation, intentional avoidance of a fracture gap was implemented, and the plate was designed to stabilize a transverse fracture on the distal one-third of the radius bone.

The condition of the radius bone after screw removal was assessed by creating several holes based on the LCP 1.5 mm notched head T-plate (length, 36.25 mm; thickness, 1.0 mm; width of head, 9 mm; width of shaft, 4.25 mm; distance between center of shaft holes, 5.0 mm, six shaft holes, Code No. VP4007.06; DePuy Synthes Companies, Raynham, MA, USA) and LCP 2.0 mm notched head T-plate (length, 54 mm; thickness, 1.33 mm; width of head, 12 mm; width of shaft, 5.0 mm; distance between center of shaft holes, 5.0 mm, seven shaft holes, Code No. VP4312.07; DePuy Synthes Companies, Raynham, MA, USA). A hollow cylinder region was determined based on the screw hole diameters of 1.5 mm (Code No. VS106.011; DePuy Synthes Companies, Raynham, MA, USA) and 2.0 mm (Code No. VS207.011; DePuy Synthes Companies, Raynham, MA, USA) locking screw. Each cylindrical structure corresponds to the respective diameter screw hole sizes, illustrating 1.5 mm and 2.0 mm, respectively. The screw hole locations were created on the radius bone, and both sections of the head hole on each plate were inserted with screw holes. Simultaneously, the shaft holes for each plate were illustrated with two different arrangements: four holes and two holes (Figure 3.2). These modifications not only replicate the screw removal process but also offer a comprehensive representation of post-surgery conditions. A normal radius without a screw hole was generated to facilitate a comparison to assess the

bone's normal condition. The resulting model enhances understanding of how different screw configurations impact the structural integrity of the radius bone.

The experimental procedures described above were performed using Simpleware ScanIP v21 (Synopsis, Sunnyvale, CA, USA). The finite element models utilized tetrahedral mesh elements with an average size of 0.2 mm. The element size for this component was selected through a rigorous analysis of convergence results, as it significantly influences the research findings. The carpal, ulna, and humerus shared identical elements and nodes for each plate model. Nevertheless, distinctions appeared when evaluating the positions of the screw holes (1.5 mm and 2.0 mm) in the radius and trabecular bones, especially in normal bone. Table 3.1 illustrates the different numbers of elements and nodes for all conditions.

3.3.3. Material properties and ligament creation

The humerus bone was represented as a homogeneous, isotropic, linearly elastic material (Synek et al. 2023). A high-resolution CT scan was conducted to differentiate between cortical and cancellous bone. Advanced image processing methods, notably thresholding and segmentation algorithms, were instrumental in accurately distinguishing cortical and cancellous bone. The subsequent verification process entailed aligning the segmented regions with different anatomical structures visible in the CT images, further substantiating this model's accuracy and biological relevance. The data from earlier studies (Hirashima et al. 2021; Lai et al. 2015; Laurent et al. 2020) were used to determine Young's modulus and Poisson's ratio of the humerus, cortical, and trabecular bone (Table 3.2). The humerus mass density was estimated by assuming that the forelimbs support 50% of the weight

of a typical toy poodle, roughly 1.5 kg. The outcome was a humeral mass density of 4.5×10^{-4} kg/mm³. Additionally, the cortical and trabecular Young's modulus, Poisson's ratio, and bone mass density data were obtained from previous research (Table 3.2) (Semb 1966).

Linear spring elements were implemented to model the biomechanical function of ligaments in connecting bones and stabilizing joints, as shown in Figure 1. These one-dimensional elastic springs produce a restoring force only when extended beyond their zero-load length, reflecting the physiological behavior of ligaments resisting tensile stress. The simplified representation allows the joint model to mimic ligament deformation under tensile loading and restrain hyperextension and dislocation. Specifically, the spring's zero-force length and stiffness properties were tuned to match the tension response of major ligamentous structures while keeping the articulating bones together within normal anisotropic limits.

3.3.4. Simulation condition

The boundary conditions were developed through the software MSC Patran v21 (Hexagon, Newport Beach, CA, USA), followed by MSC Marc Mentat v21 (Hexagon, Newport Beach, CA, USA) to conduct the analysis. The initial velocities of 2800 mm/s were specifically applied to the humerus with a 0.0025 seconds timeframe partitioned into 800 increments, encompassing the critical event of fracture occurrence at ground contact. The above initial velocities represent drop heights of 40 cm, which display the most noticeable and appropriate disparities in the fracture mechanisms observed in toy-breed canines based on the preliminary research. The decision demonstrates to recreate the real-life situations experienced

by these dogs during fall conditions, maximizing the efficiency of experimental resources and adopting an integrated approach that connects therapeutic significance with practical achievability. The carpals were fully constrained during the simulation to represent rigid contact with an unyielding ground plane. Equivalent node identifiers were systematically compiled from normal and screw-holed bone conditions, signifying the stress values. Subsequently, these data points were employed to facilitate a comprehensive comparative analysis. Von Mises stresses were determined within the radius under different loading circumstances to compare the impact of 1.5 mm and 2.0 mm LCP notched T-plate screw holes configurations on mechanical characteristics that lead to distal radius fractures.

3.3.5 Ethical approval

This study did not require ethical approval. The owners granted informed consent by completing and signing a consent form before the examination. The collected data were employed under anonymization protocols and general consent agreements.

3.4. Results

The analysis in Figure 3.3 compares von Mises stress distribution across one-third of the distal radius, considering various screw-hole locations. Regardless of screw hole configuration, LCP 2.0 mm shows a more uniform stress distribution than LCP 1.5 mm. Localized stress concentration around screw holes is consistent across all plate designs. Notably, the 4-hole shaft design exhibits the highest stress concentration at screw hole 4 for the 1.5 mm plate and screw hole 3 for the 2.0 mm plate. The 2-hole shaft design, however, displays distinct patterns, with the 1.5 mm design concentrating stress on screw

hole 2, while the 2.0 mm design has consistent stress distribution between both screw holes. Importantly, stress concentration around trabecular screw holes is consistently lower than that around shaft screw holes across all plates. The stress values at each screw hole across all plates were described in the specific data provided below.

3.4.1. Four-hole screw shaft design

The stress values within the shaft screw holes of the normal bone showed the highest stress concentration at S3, registered at 1035.02 MPa (Figure 3.4). The 1.5 mm plate resulted in elevated stress across all screw shaft locations, particularly at S4, reaching 1898.54 MPa. Similarly, the 2.0 mm plate exhibited a pronounced increase, notably at S3, where values surged from 1035.02 MPa in normal bone to 2586.39 MPa. Regarding the head screw, stress values around H1 and H2 in the normal bone were relatively lower at 86.9 MPa and 123.72 MPa, respectively. However, the 1.5 mm plate led to a marked escalation, with stress levels significantly increasing to 372.24 MPa and 332.8 MPa around H1 and H2, respectively. The 2.0 mm plate yielded elevated stress levels of 930.79 MPa and 596.50 MPa around H1 and H2, respectively.

3.4.2. Two-hole screw shaft design

The stress values within the shaft screw holes of the normal bone demonstrated that the maximum stress concentration was observed at S2, reaching 1035.02 MPa (Figure 3.5). The 1.5 mm plate screw hole increased stress at all configurations, especially at S2, where it reached 2264.78 MPa. Similar patterns were observed with the 2.0 mm plate, with stress at S2 rising from 1035.02 MPa in normal bone to 1848.36 MPa. Simultaneously when considering the head screw,

stress levels around H1 and H2 were lower in normal bone (86.90 MPa and 123.72 MPa, respectively). However, the 1.5 mm plate showed a substantial increase, reaching 384 MPa at H1 and 343.25 MPa at H2. The 2.0 mm plate design further heightened stress levels, with 760.04 MPa at H1 and 531.27 MPa at H2.

3.5. Discussion

Orthopedic veterinary practitioners frequently confront challenges and uncertainties during the post-operative phase, particularly when determining the optimal timing for the removal of screws from bone plates. FEA emerges as a sophisticated computational technique to navigate the complexities, enabling a thorough exploration of the mechanical interactions between bone and implant. The author's earlier experiment underscored concentrated stresses in the distal regions of the toy poodle's radius bones. The results align seamlessly with the present findings, reinforcing the consistent elevation of stress levels in the distal regions, as shown on the bones without holes (Figure 3.3). The current study provides important findings on the mechanical dynamics of the radius bone, with a particular emphasis on the specific examination of stress distribution around the bone screws holes. The discovered findings remarkably advance the understanding of post-operative screw removal conditions in toy-breed dogs, offering fundamental insights into veterinary orthopedics.

Plates with longer lengths showed a more uniform stress distribution on the one-third distal radius. Interestingly, an increase in the number of screw holes in the plate was associated with heightened stress concentration around specific screw holes. The author's viewpoint regarding the present outcomes was that the plate length considerably influences stress distribution on the radius. The shorter plate has a limited area for stress distribution, leading to stress accumulation at the proximal region of the screw hole. Conversely, a

longer plate enables a more uniform stress distribution. As shown by (El-Anwar and El-Zawahry 2011; Erdem et al. 2018), plate size and increased implant length would generate a uniform load distribution and improve biomechanical performance. A recent study (Wang et al. 2020; Valeri et al. 2024) similarly conveyed that various factors, including the working length of the plate, the presence of holes, the overall size of the plate, and the diameter and length of the screw, influence the mechanical environment around the bone. A recent study similarly conveyed that various factors, including the working length of the plate, the presence of holes, and the overall length of the plate, influence the mechanical environment around long bone mid-shaft fractures. In addition, the study identified that the configuration of the shaft-hole screw, as shown by the 4-hole shaft design, has a considerable effect on the stress level at a particular location. The rationale behind these results could be identified due to each screw hole insertion resulting in the removal of bone mass, diminishing the overall cross-sectional area (CSA) available for stress distribution. This condition leads to the remaining material around the screw holes being compelled to withstand an increased load, resulting in heightened stress levels. According to fundamental principles in the mechanics of materials, stress is defined as the internal force within a material divided by the CSA area over which the force acts. Following this, a diminished CSA raises stress levels when subjected to a specific applied load. Studies conducted by (Nelson et al. 2000; Zaki et al. 2015) found that the strength of long bones is mainly derived from the complex geometric details embedded in their cross-sectional structure. Bones with a larger CSA typically have greater bone mass and density. This characteristic facilitates the extensive distribution of bone tissue, enhancing its durability and capacity to endure bending or fractures. Further investigations have also indicated that bone mass and density are crucial in determining bone strength and impacting the possibility of fractures (Felder et al. 2017; Jaworski et al. 2019; Pomeroy et

al. 2018). These findings emphasize the importance of a comprehensive orthopedic strategy that considers both the mechanical stability offered by implants and their effect on the structural integrity of the bone.

Analysis of stress distribution across all plates revealed a concentrated accumulation of stress adjacent to the screw holes. These findings could be explained by the presence of screw holes, which create a structural irregularity resembling a defect in the bone. The presence of this discontinuity shape causes a disturbance in the uniform distribution of stress, leading to increased stress levels that are focused in the area surrounding the screw holes. The documented results agreed with Wolff's Law, emphasizing that bones adapt their structure in response to alterations in mechanical conditions to enhance their function (Dittmer and Firth 2017). In other words, the bone undergoes a self-reinforcement process in regions with reduced bone mass, demonstrating its continual adaptation to stress distribution. Prior experimental research has supported our results (Rosson et al. 1991), which showed that remaining screw holes have a substantial impact on bone weakening following plate removal, reducing the bone's absorbing capacity by approximately half. The weakening condition after the extraction of screws could initiate stress risers due to micro damage within the screw holes when receiving normal loads, compromising its structural integrity and heightening the risk of fractures (Velkes et al. 1966; Yoo et al. 2021; Zhou et al. 2019). Our findings also resonate with (Largura et al. 2014), which states that a greater magnitude of deformations developed at a close distance to the point of screw application. Similarly, (Bologna et al. 2023) discovered elevated stress levels in areas surrounding the screw holes when evaluating the maximum stress and fatigue life of bone plates under in vivo loads.

The trabeculae region presented with the lowest amount of stress around the screw holes in comparison to the shaft screw holes on all plates. The author presumed that the

variance in Young's modulus between cortical and trabecular bone might be associated with the different stress distributions. Cortical bone resists substantial elastic deformation under stress with its higher Young's modulus. In contrast, the trabecular bone's lower modulus allows for more significant elastic deformation and promotes a uniform stress distribution around screw holes. Existing evidence aligns with the findings (Almer and Stock 2007; J. Currey 2004; J. D. Currey 2004), indicating a positive correlation between the increase of Young's modulus in the cortical region and elevated stress along the bone. The observed phenomenon in the clinical condition can be attributed to the distinctive anatomical characteristics of trabecular bone. This region is designed with larger dimensions and a supportive network that efficiently distributes and absorbs stresses, surpassing cortical bone in the diaphyseal region. The porous structure of trabecular bone allows for superior stress distribution (Oftadeh et al. 2015), making it well-suited to accommodate the forces associated with screw removal without creating localized stress points. Conversely, the cortical bone of the diaphyseal shaft, which has a significantly reduced porosity and less effective stress dissipation capabilities, resulted in the accumulation of stress, specifically adjacent to the screw hole. Remarkably, numerous FEA studies (Barão et al. 2013; Cicciù et al. 2018; Kim et al. 2023; Vijayalakshmi et al. 2012; Zhang et al. 2023) have substantiated these clinical findings, consistently demonstrating that the trabecular region exhibits lower stress concentrations compared to the cortical region. The convergence of clinical observations and FEA outcomes underscores the robustness of trabecular bone's distinctive anatomical characteristics in providing superior stress distribution.

The current study has some limitations that should be acknowledged. Illustrating the complex interplay of anatomical features and physiological reactions in clinical scenarios, including the recreation of intricate biomechanics in the elbow and shoulder

joints and simulating the complex muscle cushioning effects in FEA, poses a highly complex and challenging task. The authors intentionally excluded these complexities to align with study objectives, acknowledging the necessary compromise between model intricacy and practical feasibility for achieving streamlined and relevant results.

3.6. Conclusion

Based on the data derived from this study, the longer plate design demonstrates superior and more uniformly distributed stress on the radius. Nevertheless, it is essential to note that there was a consistent observation of localized stress close to the screw holes. The findings underscore the importance of considering plate length and screw arrangement when evaluating stress distribution on the radius, especially in toy-breed dogs. This perceptive understanding substantially advances the comprehension of the dynamics associated with post-operative screw removal, offering invaluable insights for more informed clinical decision-making processes.

3.7. Table chapter III

Table. 3.1. Number of each element and nodes of each model.

Model	Element				Nodes			
	1.5 mm		2.0 mm		1.5 mm		2.0 mm	
	A	B	A	B	A	B	A	B
Humerus	41147				7106			
Ulna	15160				3828			
Carpal	6452				2050			
Trabecular	6137	6042	3259	3036	2785	2258	980	878
Radius	28575	27498	32639	31450	9120	8834	10470	10087

Table. 3.2. Physical properties of bone material.

Element	Young Modulus (MPa)	Poisson's ratio	Mass density (kg/mm^3)
Humerus	17000	0.3	4.5×10^{-4}
Cortical	17000	0.3	2.1×10^{-6}
Trabecular	350	0.3	7.0×10^{-7}

3.8. Figure chapter III

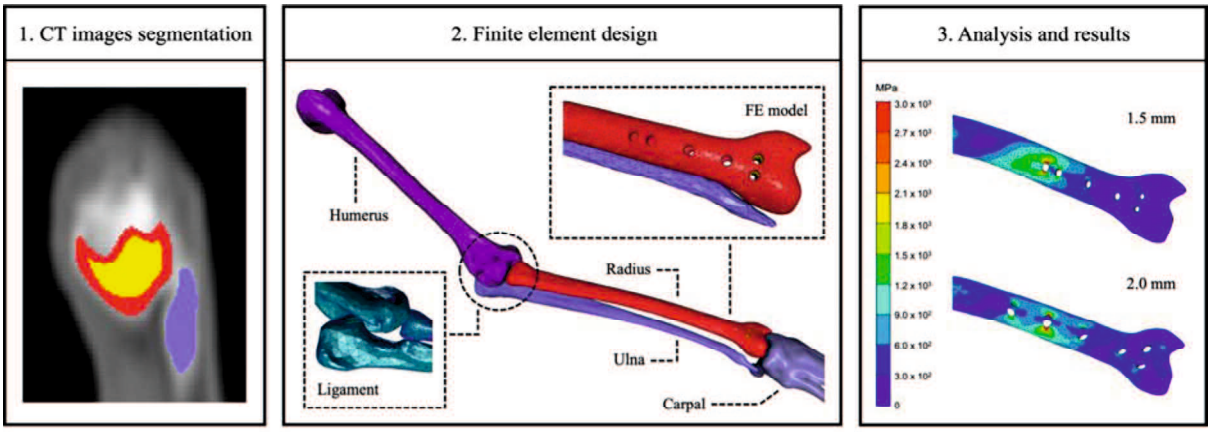

Figure 3.1. Finite element design.

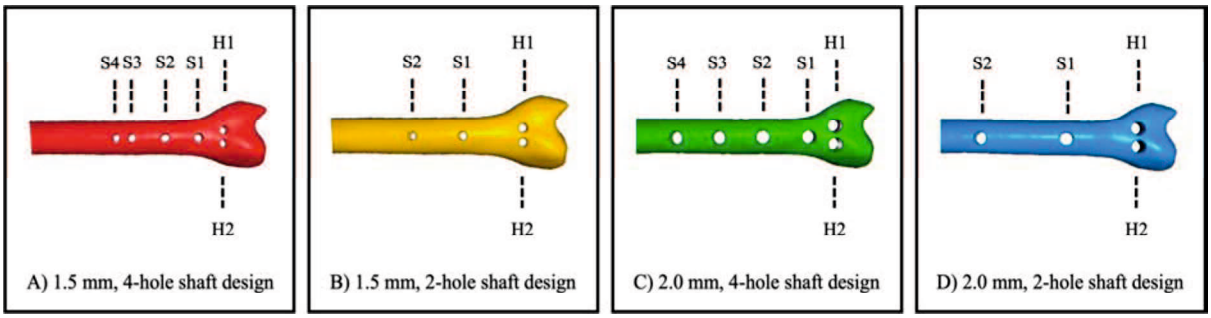

Figure 3.2. Screw-hole arrangement on each plate. Head screw hole 1 (H1), head screw hole 2 (H2), shaft screw hole 1 (S1), shaft screw hole 2 (S2), shaft screw hole 3 (S3), shaft screw hole 4 (S4).

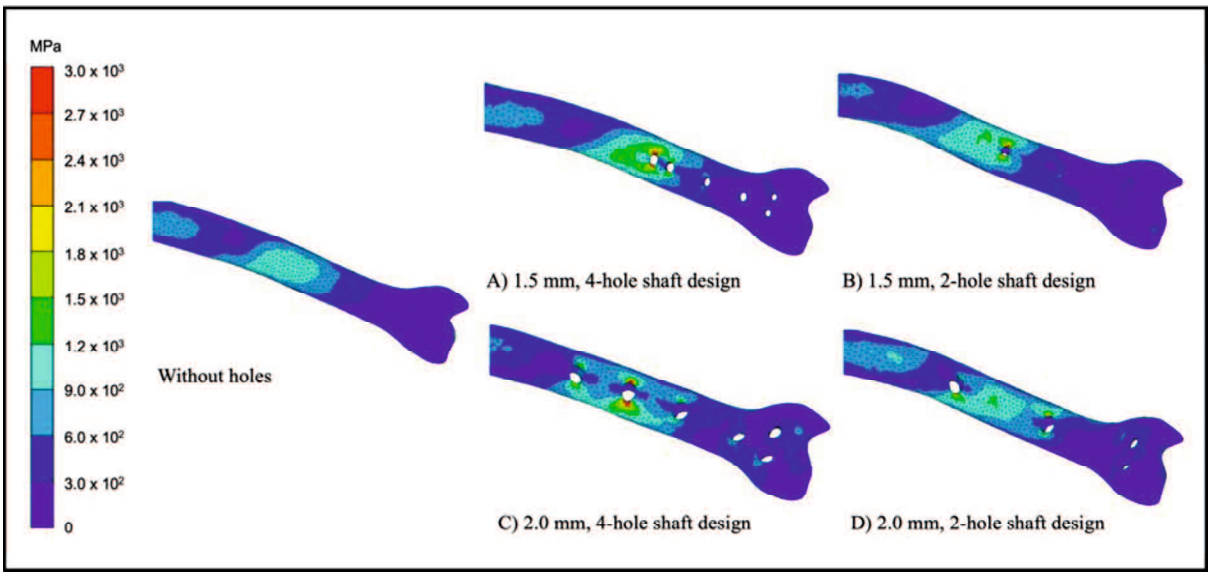

Figure 3.3. Comparison of stress distribution with varying screw hole locations. The stress levels were illustrated using a color scale, where red signifies the most elevated stress zone.

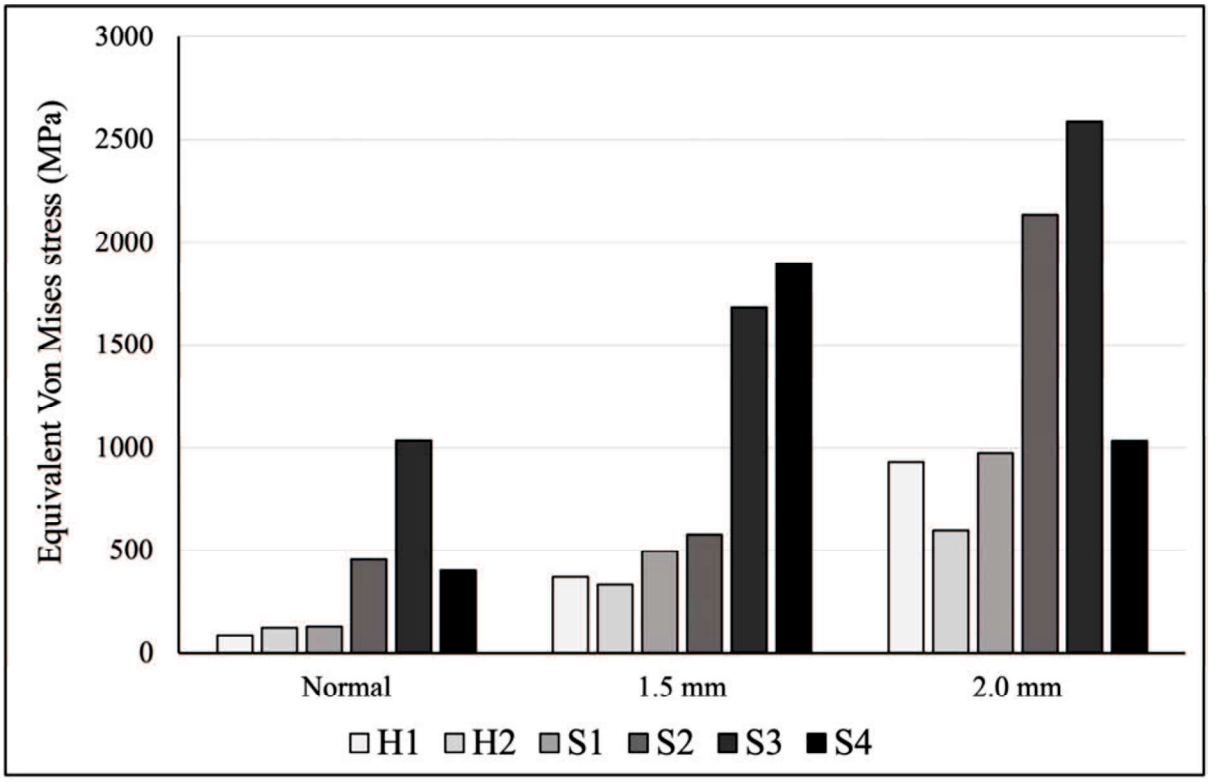

Figure 3.4. Bar graph comparison of stress distribution on 4-hole screw shaft design.

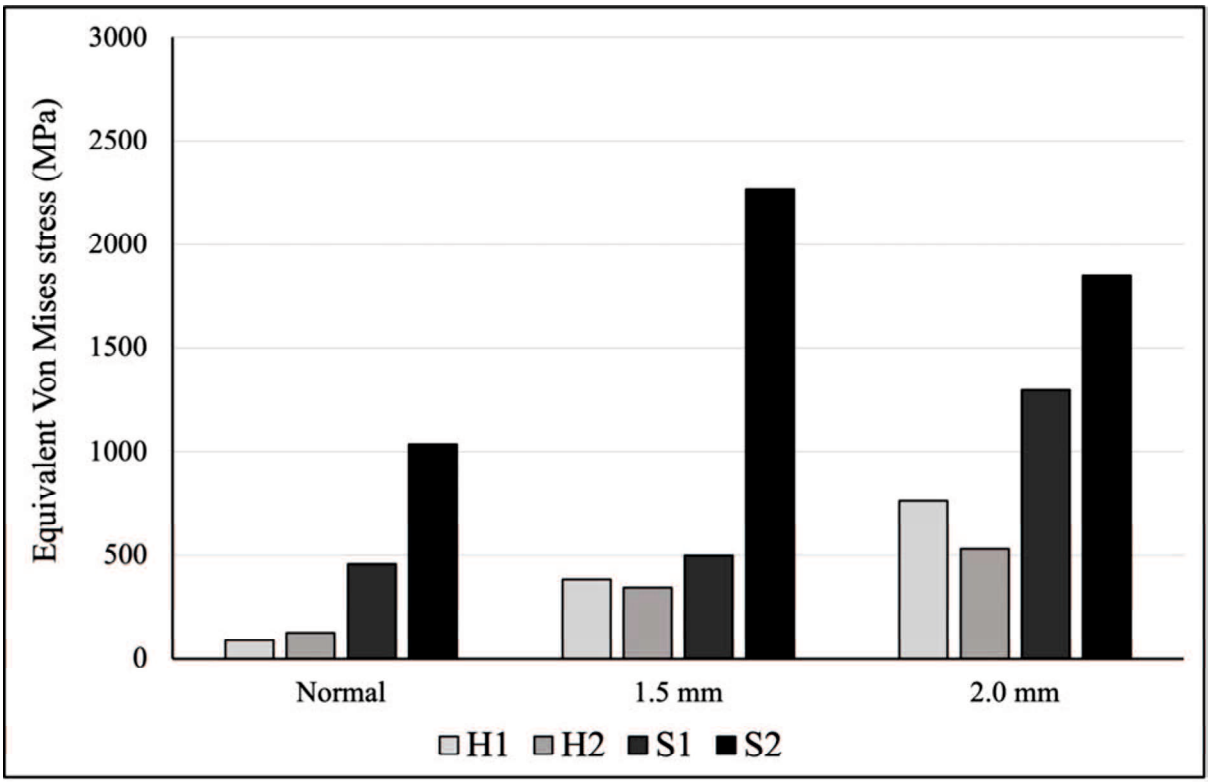

Figure 3.5. Bar graph comparison of stress distribution on 2-hole screw shaft design.

ACKNOWLEDGMENT

I am deeply grateful to the esteemed individuals and institutions who have integrally completed my doctoral research. The studies have been conducted at the Laboratory of Veterinary Surgery, Animal Medical Centre, Joint Graduate School of Veterinary Medicine, Yamaguchi University, Japan, and the Department of Mechanical Engineering, Graduate School of Sciences and Technology for Innovation, Yamaguchi University, Japan, spanning the years 2020 to 2024.

I am deeply grateful to express my utmost appreciation to my principal supervisor, Prof. Dr. Kenji Tani. His exceptional guidance, invaluable insights, and support have been instrumental throughout my study. Professor Tani's mentorship has been instrumental in shaping the course of my studies and significantly contributing to the success and fulfillment of my research endeavors. His profound expertise, encouragement, and unwavering commitment to my intellectual development have constituted the foundational elements of my academic pursuits. I sincerely appreciate the opportunity to work under his guidance; his esteemed leadership has unquestionably impacted my academic endeavor's progress.

I would like to express my sincere gratitude to Prof. Fei Jiang, Ph.D., for graciously imparting his expertise and providing invaluable assistance in introducing finite element analysis to my veterinary orthopedics research at the Department of Mechanical Engineering. His collaboration has significantly enriched the interdisciplinary aspects of my work.

I extend my sincere gratitude to the esteemed teachers at Yamaguchi University Animal Medical Centre, Dr. Hiroshi Sunahara, Dr. Harumichi Itoh, Prof. Dr. Munekazu Nakaichi, Dr. Hiro Horikirizono, and Dr. Yuki Nemoto. Their guidance, teachings, and generous provision of opportunities for hands-on experience within the animal hospital have contributed to my academic journey. I would like to express special appreciation to Dr. Kazuhito Itamoto, who

first introduced me and allowed me to join his class in veterinary anesthesia. This particular academic experience stands out as the best among my studies at the animal hospital, and I am grateful for the valuable insights I gained.

I wish to convey my sincere appreciation to Japan's Ministry of Education, Culture, Sports, Science and Technology (Monbukagakusho) for their financial support, which has been pivotal in successfully executing my research endeavors.

My deepest thanks are extended to my father, Sudibyo Martono, and my mother, Setyalastuti, for their support, encouragement, and prayers throughout this academic pursuit. Their steadfast belief in my abilities has been an enduring source of inspiration.

Finally, my heartfelt thanks go to all the students and veterinary technicians at Yamaguchi University Animal Medical Centre (YUAMEC) who have been instrumental in providing indispensable assistance and support during my tenure at the hospital. I express profound gratitude to those individuals who have played instrumental roles in facilitating my acquisition of the Japanese language and fostering a collaborative and inclusive learning environment. Upon my initial arrival at the hospital, I encountered a significant language barrier as I was unable to communicate effectively in Japanese. With immense appreciation, I acknowledge this community's invaluable assistance and support, which have contributed significantly to my language learning journey.

This dissertation serves as evidence of the collective efforts and support of these esteemed individuals and institutions. Without all the consistent assistance, this academic milestone would not have been attainable, and I am profoundly grateful for this.

REFERENCES

Abu-Hammad, O., Khraisat, A., Dar-Odeh, N. and El-Maaytah, M. (2007). Effect of dental implant cross-sectional design on cortical bone structure using finite element analysis. *Clinical Implant Dentistry and Related Research*, 9(4), pp.217–221.

Agyapong-Badu, S., Warner, M., Samuel, D. and Stokes, M. (2016). Measurement of ageing effects on muscle tone and mechanical properties of rectus femoris and biceps brachii in healthy males and females using a novel hand-held myometric device. *Archives of Gerontology and Geriatrics*, 62, pp.59–67.

Aikawa, T., Miyazaki, Y., Shimatsu, T., Iizuka, K. and Nishimura, M. (2018). Clinical Outcomes and Complications after Open Reduction and Internal Fixation Utilizing Conventional Plates in 65 Distal Radial and Ulnar Fractures of Miniature- and Toy-Breed Dogs. *Veterinary and Comparative Orthopaedics and Traumatology*, 31(3), pp.214–217.

Alderson, B., Mark Senior, J., Jones, R.S. and Dugdale, A.H. (2007). Use of rocuronium administered by continuous infusion in dogs. *Veterinary Anaesthesia and Analgesia*, 34(4), pp.251–256.

Almer, J.D. and Stock, S.R. (2007). Micromechanical response of mineral and collagen phases in bone. *Journal of Structural Biology*, 157(2), pp.365–370.

Alwen, S.G.J., Kapatkin, A.S., Garcia, T.C., Milgram, J. and Stover, S.M. (2018). Open screw placement in a 1.5 mm LCP over a fracture gap decreases fatigue life. *Frontiers in Veterinary Science*, 5, pp.1–8.

ANICOM. (2023). *White paper on household animals*. *https://www.anicom-page.com/hakusho/book/pdf/book_202312.pdf*.

Appiah-Ankam, J. and Hunter, J.M. (2004). Pharmacology of neuromuscular blocking drugs. *Continuing Education in Anaesthesia, Critical Care and Pain*, 4(1), pp.2–7.

De Arburn Parent, R., Benamou, J., Gatineau, M., Clerfond, P. and Planté, J. (2017). Open reduction and cranial bone plate fixation of fractures involving the distal aspect of the radius and ulna in miniature- and toy-breed dogs: 102 cases (2008–2015). *Journal of the American Veterinary Medical Association*, 250(12), pp.1419–1426.

Arias-Moreno, A.J., Ito, K. and van Rietbergen, B. (2020). Accuracy of beam theory for estimating bone tissue modulus and yield stress from 3-point bending tests on rat femora. *Journal of Biomechanics*, 101, pp.1–8.

Auer, U. (2007). Clinical observations on the use of the muscle relaxant rocuronium bromide in the dog. *Veterinary Journal*, 173(2), pp.422–427.

Barão, V.A.R., Delben, J.A., Lima, J., Cabral, T. and Assunção, W.G. (2013). Comparison of different designs of implant-retained overdentures and fixed full-arch implant-supported prosthesis on stress distribution in edentulous mandible - A computed tomography-based three-dimensional finite element analysis. *Journal of Biomechanics*, 46(7), pp.1312–1320.

Bell, A.L., Rozanski, E.A. and Babyak, J. (2022). A multicenter retrospective comparison of trauma in toy breeds versus giant breeds: A Veterinary Committee on Trauma registry study. *Journal of Veterinary Emergency and Critical Care*, 32(1), pp.26–33.

Berko, N.S., Mehta, A.K., Levin, T.L. and Schulz, J.F. (2015). Effect of knee position on the ultrasound elastography appearance of the patellar tendon. *Clinical Radiology*, 70(10), pp.1083–1086.

Biskup, J., Freeman, A., Camisa, W., Innes, J. and Conzemius, M. (2014). Mechanical Properties of Canine Patella-Ligament-Tibia Segment. *Veterinary Surgery*, 43(2), pp.136–141.

Bohm, S., Mersmann, F. and Arampatzis, A. (2015). Human tendon adaptation in response to mechanical loading: a systematic review and meta-analysis of exercise intervention studies on healthy adults. *Sports Medicine - Open*, 1(7), pp.1–18.

Bologna, F.A., Audenino, A.L. and Terzini, M. (2023). An analytical and in silico strategy for estimating maximum stress and fatigue life of bone plates under in vivo loads: a rationale for regulatory testing. *Frontiers in Medical Engineering*, 1, pp.1–9.

Boudrieau R.J. (2003). Fractures of the radius and ulna. In: *Textbook of small animal surgery*. 3rd ed. Philadelphia: W.B. Saunders, pp.1953–1973.

Bravo-Sánchez, A., Abián, P., Sánchez-Infante, J., Ramírez-delaCruz, M., Esteban-García, P., Jiménez, F. and Abián-Vicén, J. (2022). Five-Compressions Protocol as a Valid Myotonometric Method to Assess the Stiffness of the Lower Limbs: A Brief Report. *International Journal of Environmental Research and Public Health*, 19(21), pp.1–7.

Brianza, S.Z.M., D'Amelio, P., Pugno, N., Delise, M., Bignardi, C. and Isaia, G. (2007). Allometric scaling and biomechanical behavior of the bone tissue: An experimental intraspecific investigation. *Bone*, 40(6), pp.1635–1642.

Brianza, S.Z.M., Delise, M., Maddalena Ferraris, M., D'Amelio, P. and Botti, P. (2006). Cross-sectional geometrical properties of distal radius and ulna in large, medium and toy breed dogs. *Journal of Biomechanics*, 39(2), pp.302–311.

Bruce WJ. (2006). Manual of Small Animal Fracture Repair and Management. In: Coughlan A and Miller A, eds. *BSAVA Manual of Small Animal Fracture Repair and Management*. 2nd ed. pp.177–196.

Burgio, V., Civera, M., Reinoso, M.R., Pizzolante, E., Prezioso, S., Bertuglia, A. and Surace, C. (2022). Mechanical Properties of Animal Tendons: A Review and Comparative Study for the Identification of the Most Suitable Human Tendon Surrogates. *Processes*, 10(3), pp.1–20.

Casagrande, D.J., Morris, R.P., Carayannopoulos, N.L. and Buford, W.L. (2016). Relationship Between Ulnar Variance, Cortical Bone Density, and Load to Failure in the Distal Radius at the Typical Site of Fracture Initiation. *Journal of Hand Surgery*, 41(12), pp.e461–e468.

de Cassia Marqueti, R., Vieira de Sousa Neto, I., Reichert Barin, F. and Vieira Ramos, G. (2019). Exercise and Tendon Remodeling Mechanism. In: *Tendons*. IntechOpen, pp.1–20.

Chaudhuri, O., Cooper-White, J., Janmey, P.A., Mooney, D.J. and Shenoy, V.B. (2020). Effects of extracellular matrix viscoelasticity on cellular behaviour. *Nature*, 584(7822), pp.535–546.

Chen, G., Liu, Z., Zhang, Y., Zhang, J., Cui, F. and Xu, M. (2016). Biomechanical Assessment for Healing Progression of Fractured Long Bones: Comparisons of Various Methods Using Beam Models. *International Journal of Applied Mechanics*, 8(6), pp.1–20.

Chen, Guoqian, Wu, J., Chen, Guocai, Lu, Y., Ren, W., Xu, W., Xu, X., Wu, Z., Guan, Y., Zheng, Y. and Qiu, B. (2019). Reliability of a portable device for quantifying tone and stiffness of quadriceps femoris and patellar tendon at different knee flexion angles. *PLoS ONE*, 14(7), pp.1–17.

Cheong, V.S. and Bull, A.M.J. (2015). A novel specimen-specific methodology to optimise the alignment of long bones for experimental testing. *Journal of Biomechanics*, 48(16), pp.4317–4321.

Cicciù, M., Cervino, G., Milone, D. and Risitano, G. (2018). FEM investigation of the stress distribution over mandibular bone due to screwed overdenture positioned on dental implants. *Materials*, 11(9), pp.1–17.

Clayton, R.A.E., Gaston, M.S., Ralston, S.H., Court-Brown, C.M. and McQueen, M.M. (2009). Association between decreased bone mineral density and severity of distal radial fractures. *Journal of Bone and Joint Surgery*, 91(3), pp.613–619.

Currey, J. (2004). Incompatible mechanical properties in compact bone. *Journal of Theoretical Biology*, 231(4), pp.569–580.

Currey, J.D. (2004). Tensile yield in compact bone is determined by strain, post-yield behaviour by mineral content. *Journal of Biomechanics*, 37(4), pp.549–556.

Dittmer, K.E. and Firth, E.C. (2017). Mechanisms of bone response to injury. *Journal of Veterinary Diagnostic Investigation*, 29(4), pp.385–395.

Dugdale MA, A.H., Adams, W.A. and Jones OBE, R.S. (2002). The clinical use of the neuromuscular blocking agent rocuronium in dogs. *Veterinary Anaesthesia and Analgesia*, 29(1), pp.49–53.

Edwards, W.B. and Troy, K.L. (2012). Finite element prediction of surface strain and fracture strength at the distal radius. *Medical Engineering and Physics*, 34(3), pp.290–298.

El-Anwar, M.I. and El-Zawahry, M.M. (2011). A three dimensional finite element study on dental implant design. *Journal of Genetic Engineering and Biotechnology*, 9(1), pp.77–82.

Erdem, S., Gür, M. and Kaman, M.O. (2018). Static and dynamic analyses of fracture fixation bone-plate systems for different plate materials and dimensions. *Bio-Medical Materials and Engineering*, 29(5), pp.611–628.

Felder, A.A., Phillips, C., Cornish, H., Cooke, M., Hutchinson, J.R. and Doube, M. (2017). Secondary osteons scale allometrically in mammalian humerus and femur. *Royal Society Open Science*, 4(11), pp.1–17.

Finni, T., de Brito Fontana, H. and Maas, H. (2023). Force transmission and interactions between synergistic muscles. *Journal of Biomechanics*, 152, pp.1–11.

Freedman, B.R., Rodriguez, A.B., Leiphart, R.J., Newton, J.B., Ban, E., Sarver, J.J., Mauck, R.L., Shenoy, V.B. and Soslowsky, L.J. (2018). Dynamic Loading and Tendon Healing

Affect Multiscale Tendon Properties and ECM Stress Transmission. *Scientific Reports*, 8(1), pp.1–13.

Freeman, B.L. (2022). A multi-point constraint unfitted finite element method. *Advanced Modeling and Simulation in Engineering Sciences*, 9(19), pp.1–22.

Frost, H.M. (2003). Bone's mechanostat: A 2003 update. *The Anatomical Record Part A: Discoveries in Molecular, Cellular, and Evolutionary Biology*, 275A(2), pp.1081–1101.

Gibert, S., Ragetly, G.R. and Boudrieau, R.J. (2015). Locking compression plate stabilization of 20 distal radial and ulnar fractures in toy and miniature breed dogs. *Veterinary and Comparative Orthopaedics and Traumatology*, 28(6), pp.441–447.

Haaland, P.J., Sjöström, L., Devor, M. and Haug, A. (2009). Appendicular fracture repair in dogs using the locking compression plate system: 47 cases. *Veterinary and Comparative Orthopaedics and Traumatology*, 22(4), pp.309–315.

Hara, T., Tanck, E., Homminga, J. and Huiskes, R. (2002). The influence of microcomputed tomography threshold variations on the assessment of structural and mechanical trabecular bone properties. *Bone*, 31(1), pp.107–109.

Hardy, A., Rodaix, C., Vergari, C. and Vialle, R. (2017). Normal Range of Patellar Tendon Elasticity Using the Sharewave Elastography Technique: An In Vivo Study in Normal Volunteers. *Surgical Technology International*, 31, pp.1–7.

Haut, R.C., Lancastert, R.L. and Decamps, C.E. (1992). Mechanical properties of the canine patellar tendon: some correlations with age and the content of collagen. *Journal of Biomechanics*, 25(2), pp.163–173.

Hingorani, R. V, Provenzano, P.P., Lakes, R.S., Escarcega, A. and Vanderby, R. (2004). Nonlinear Viscoelasticity in Rabbit Medial Collateral Ligament. *Annals of Biomedical Engineering*, 32(2), pp.306–312.

Hirashima, T., Matsuura, Y., Suzuki, T., Akasaka, T., Kanazuka, A. and Ohtori, S. (2021). Long-term Evaluation Using Finite Element Analysis of Bone Atrophy Changes after Locking Plate Fixation of Forearm Diaphyseal Fracture. *Journal of Hand Surgery Global Online*, 3(5), pp.240–244.

Holcombe, S.A., Kang, Y.S., Derstine, B.A., Wang, S.C. and Agnew, A.M. (2019). Regional maps of rib cortical bone thickness and cross-sectional geometry. *Journal of Anatomy*, 235(5), pp.883–891.

Huang, C. and Ogawa, R. (2010). Mechanotransduction in bone repair and regeneration. *The FASEB Journal*, 24(10), pp.3625–3632.

Javier Núñez, F., Carlos Martínez, J., Overberg, J.-A., Torreno, N. and Suarez-Arrones, L. (2023). Hamstring muscle architecture and myotonometer measurements in elite professional football players with a prior strained hamstring. *Biology of Sport*, 40(1), pp.93–99.

Jaworski, M., Wierzbicka, E., Pludowski, P. and Szalecki, M. (2019). Forearm bone density, cross-sectional size and muscle cross-sectional area in adolescents with diabetes mellitus type 1 assessed by peripheral quantitative computed tomography. *Journal of Musculoskeletal and Neuronal Interactions*, 19(4), pp.435–447.

Johnson, J.E. and Troy, K.L. (2017). Validation of a new multiscale finite element analysis approach at the distal radius. *Medical Engineering and Physics*, 44, pp.16–24.

Kang, B.J., Ryu, H.H., Park, S., Kim, Y., Kweon, O.K. and Hayashi, K. (2016). Clinical evaluation of a mini locking plate system for fracture repair of the radius and ulna in miniature breed dogs. *Veterinary and Comparative Orthopaedics and Traumatology*, 29(6), pp.522–527.

Kim, J., Chun, B.J. and Kim, J.J. (2023). Quantitative Load Dependency Analysis of Local Trabecular Bone Microstructure to Understand the Spatial Characteristics in the Synthetic Proximal Femur. *Biology*, 12(2), pp.1–21.

Klich, S., Krymski, I. and Kawczynski, A. (2020). Viscoelastic properties of lower extremity muscles after elite track cycling sprint events: A case report. *Central European Journal of Sport Sciences and Medicine*, 29(1), pp.5–10.

Kneifel, P., Moewis, P., Damm, P., Schütz, P., Dymke, J., Taylor, W.R., Duda, G.N. and Trepczynski, A. (2023). Patellar tendon elastic properties derived from in vivo loading and kinematics. *Journal of Biomechanics*, 151, pp.1–9.

Ko, C.Y., Choi, H.J., Ryu, J. and Kim, G. (2018). Between-day reliability of MyotonPRO for the non-invasive measurement of muscle material properties in the lower extremities of patients with a chronic spinal cord injury. *Journal of Biomechanics*, 73, pp.60–65.

Kongsgaard, M., Reitelseder, S., Pedersen, T.G., Holm, L., Aagaard, P., Kjaer, M. and Magnusson, S.P. (2007). Region specific patellar tendon hypertrophy in humans following resistance training. *Acta Physiologica*, 191(2), pp.111–121.

Kontulainen, S., Liu, D., Manske, S., Jamieson, M., Sievänen, H. and McKay, H. (2007). Analyzing Cortical Bone Cross-Sectional Geometry by Peripheral QCT: Comparison With Bone Histomorphometry. *Journal of Clinical Densitometry*, 10(1), pp.86–92.

Kuervers, E.J., Firminger, C.R. and Edwards, W.B. (2021). Effect of Knee Angle and Quadriceps Muscle Force on Shear-Wave Elastography Measurements at the Patellar Tendon. *Ultrasound in Medicine and Biology*, 47(8), pp.2167–2175.

Lai, Y.S., Chen, W.C., Huang, C.H., Cheng, C.K., Chan, K.K. and Chang, T.K. (2015). The effect of graft strength on knee laxity and graft in-situ forces after posterior cruciate ligament reconstruction. *PLoS ONE*, 10(5), pp.1–11.

Lange, J.R. and Fabry, B. (2013). Cell and tissue mechanics in cell migration. *Experimental Cell Research*, 319(16), pp.2418–2423.

LaPrade, M.D., Kallenbach, S.L., Aman, Z.S., Moatshe, G., Storaci, H.W., Turnbull, T.L., Arendt, E.A., Chahla, J. and LaPrade, R.F. (2018). Biomechanical Evaluation of the Medial Stabilizers of the Patella. *American Journal of Sports Medicine*, 46(7), pp.1575–1582.

Largura, L.Z., Argenta, M.A., Sakima, M.T., Camargo, E.S., Guariza-Filho, O. and Tanaka, O.M. (2014). Bone stress and strain after use of a miniplate for molar protraction and uprighting: A 3-dimensional finite element analysis. *American Journal of Orthodontics and Dentofacial Orthopedics*, 146(2), pp.198–206.

Laurent, C.P., Böhme, B., Verwaerde, J., Papeleux, L., Ponthot, J.P. and Balligand, M. (2020). Effect of orthopedic implants on canine long bone compression stiffness: a combined experimental and computational approach. *Proceedings of the Institution of Mechanical Engineers, Part H: Journal of Engineering in Medicine*, 234(3), pp.255–264.

Lee, D. V., Bertram, J.E.A. and Todhunter, R.J. (1999). Acceleration and balance in trotting dogs. *Journal of Experimental Biology*, 202(24), pp.3565–3573.

Lill, C.A., Goldhahn, J., Albrecht, A., Eckstein, F., Gatzka, C. and Schneider, E. (2003). Impact of Bone Density on Distal Radius Fracture Patterns and Comparison between Five Different Fracture Classifications. *Journal of Orthopaedic Trauma*, 17(4), pp.271–278.

Liu, C.L., Li, Y.P., Wang, X.Q. and Zhang, Z.J. (2018). Quantifying the stiffness of achilles tendon: Intra-and inter-operator reliability and the effect of ankle joint motion. *Medical Science Monitor*, 24, pp.4876–4881.

Louis, O., Cattrysse, E., Scafoglieri, A., Luypaert, R., Clarys, J.P. and De Mey, J. (2010). Accuracy of Peripheral Quantitative Computed Tomography and Magnetic Resonance

Imaging in Assessing Cortical Bone Cross-Sectional Area: A Cadaver Study. *Journal of Computer Assisted Tomography*, 34(3), pp.469–472.

Lozano, P.F., Scholze, M., Babian, C., Scheidt, H., Vielmuth, F., Waschke, J., Ondruschka, B. and Hammer, N. (2019). Water-content related alterations in macro and micro scale tendon biomechanics. *Scientific Reports*, 9(1), pp.1–12.

Mancuso, M.E., Johnson, J.E., Ahmed, S.S., Butler, T.A. and Troy, K.L. (2018). Distal radius microstructure and finite element bone strain are related to site-specific mechanical loading and areal bone mineral density in premenopausal women. *Bone Reports*, 8, pp.187–194.

Martin, H., Gutteck, N., Matthies, J.B., Hanke, T., Gradl, G., Wohlrab, D., Mittlmeier, T. and Grabow, N. (2015). Possible reasons for early artificial bone failure in biomechanical tests of ankle arthrodesis systems. *Current Directions in Biomedical Engineering*, 1(1), pp.507–509.

Martin-Flores, M., Sakai, D.M., Campoy, L. and Gleed, R.D. (2018). Survey of how different groups of veterinarians manage the use of neuromuscular blocking agents in anesthetized dogs. *Veterinary Anaesthesia and Analgesia*, 45(4), pp.443–451.

Masic, A., Bertinetti, L., Schuetz, R., Chang, S.W., Metzger, T.H., Buehler, M.J. and Fratzl, P. (2015). Osmotic pressure induced tensile forces in tendon collagen. *Nature Communications*, 6, pp.2–8.

McCagherty, J., Longo, M., Pennington, C., Liuti, T., Morrison, L.R., Brown, H. and Clements, D.N. (2020). Effect of Stifle Flexion Angle on the Repeatability of Real-Time Elastosonography of the Patellar Ligament in Medium- To Large-Breed Dogs. *Veterinary and Comparative Orthopaedics and Traumatology*, 33(6), pp.391–397.

McCartney, W., Kiss, K. and Robertson, I. (2010). Treatment of distal radial/ulnar fractures in 17 toy breed dogs. *Veterinary Record*, 166(14), pp.430–432.

Mejia, S., Iodence, A., Griffin, L., Withrow, S., Puttlitz, C., Salman, M. and Seguin, B. (2019). Comparison of cross-sectional geometrical properties and bone density of the proximal radius between Saint Bernard and other giant breed dogs. *Veterinary Surgery*, 48(6), pp.947–955.

Mersmann, F., Pentidis, N., Tsai, M.S., Schroll, A. and Arampatzis, A. (2019). Patellar tendon strain associates to tendon structural abnormalities in adolescent athletes. *Frontiers in Physiology*, 10, pp.1–10.

Motamed, C. (2023). Intraoperative Monitoring of Neuromuscular Blockade. *Life*, 13(5), pp.1–13.

de Moya, K. and Kim, S. (2020). Radiographic evaluation of patellar tendon length following corrective surgical procedures for medial patellar luxation in dogs. *PLoS ONE*, 15(9), pp.1–7.

Nakatsuchi, H., Tadano, S., Todoh, M., Nakatsuchi, Y., Mori, S. and Endo, M. (2006). Finite Element Modeling of the Cortical Bone Region Using Clinical CT Images. *Journal of Biomechanical Science and Engineering*, 1(2), pp.316–326.

Nelson, D.A., Barondess, D.A., Hendrix, S.L. and Beck, T.J. (2000). Cross-sectional geometry, bone strength, and bone mass in the proximal femur in black and white postmenopausal women. *Journal of Bone and Mineral Research*, 15(10), pp.1992–1997.

Oftadeh, R., Perez-Viloria, M., Villa-Camacho, J.C., Vaziri, A. and Nazarian, A. (2015). Biomechanics and Mechanobiology of Trabecular Bone: A Review. *Journal of Biomechanical Engineering*, 137(1), pp.1–15.

Okamura, N., Tsukune, M., Kobayashi, Y., Sugano, S. and Fujie, M.G. (2015). Investigation of the Effect of Joint Angle on Muscle Hardness in Static Stretching of the Gastrocnemius. In: *Proceedings of the 6th International Conference on Advanced Mechatronics (ICAM2015)*. pp.267–268.

Pearson, S.J., Mohammed, A.S.A. and Hussain, S.R. (2017). Patellar tendon in vivo regional strain with varying knee angle. *Journal of Biomechanics*, 61, pp.45–50.

Piccionello, A.P., Serrani, D., Busoni, V., Salvaggio, A., Bonazzi, M., Bergamino, C. and Volta, A. (2018). Sonoelastographic Features of the Patellar Ligament in Clinically Normal Dogs. *Veterinary and Comparative Orthopaedics and Traumatology*, 31(4), pp.279–284.

Plassais, J., Rimbault, M., Williams, F.J., Davis, B.W., Schoenebeck, J.J. and Ostrander, E.A. (2017). Analysis of large versus small dogs reveals three genes on the canine X chromosome associated with body weight, muscling and back fat thickness. *PLoS Genetics*, 13(3), pp.1–20.

Pomeroy, E., Macintosh, A., Wells, J.C.K., Cole, T.J. and Stock, J.T. (2018). Relationship between body mass, lean mass, fat mass, and limb bone cross-sectional geometry: Implications for estimating body mass and physique from the skeleton. *American Journal of Physical Anthropology*, 166(1), pp.56–69.

Popovici, C.P., Mircean, M., Scurtu, I., Ober, C., Pestean, C., Sevastre, B. and Oana, L. (2014). Rocuronium Use in Anaesthetics Protocol in Canine Patients with Orthopedic Disease. *Bulletin UASVM Veterinary Medicine*, 71(2), pp.462–466.

Pownder, S.L., Hayashi, K., Lin, B.Q., Meyers, K.N., Caserto, B.G., Breighner, R.E., Potter, H.G. and Koff, M.F. (2021). Differences in the magnetic resonance imaging parameter T2* may be identified during the course of canine patellar tendon healing: a pilot study. *Quantitative Imaging in Medicine and Surgery*, 11(4), pp.1234–1246.

Pozarowszczyk, B., Pawlaczyk, W., Smoter, M., Zarzycki, A., Mroczek, D., Kumorek, M., Witkowski, K. and Adam, K. (2017). Effects of Karate Fights on Achilles Tendon Stiffness Measured by Myotonometry. *Journal of Human Kinetics*, 56(1), pp.93–97.

Pramudita, J.A., Hiroki, W., Yoda, T. and Tanabe, Y. (2022). Variations in Strain Distribution at Distal Radius under Different Loading Conditions. *Life*, 12(5), pp.1–12.

Rajaai, S.M., Pourakbar Saffar, K. and Jamilpour, N. (2010). Mechanical Properties of Long Bone Shaft in Bending. In: *XII Mediterranean Conference on Medical and Biological Engineering and Computing*. Berlin, Heidelberg.: Springer, pp.729–732.

Ramazanoglu, E., Turhan, B. and Usgu, S. (2021). Evaluation of the tone and viscoelastic properties of the masseter muscle in the supine position, and its relation to age and gender. *Dental and Medical Problems*, 58(2), pp.155–161.

Rao, Z.-T., Yuan, F., Li, B. and Ma, N. (2014). Effect of elbow flexion angles on stress distribution of the proximal ulnar and radius bones under a vertical load: measurement using resistance strain gauges. *Journal of Orthopaedic Surgery and Research*, 9(60), pp.1–7. Available from: http://www.josr-online.com/content/9/1/60.

Revel, M., Bermond, F., Mitton, D. and Follet, H. (2020). Specimen-specific finite element prediction of surface strain at the distal radius in a fall configuration. *Computer Methods in Biomechanics and Biomedical Engineering*, 23(sup1), pp.S257–S259.

Rimbault, M. and Ostrander, E.A. (2012). So many doggone traits: Mapping genetics of multiple phenotypes in the domestic dog. *Human Molecular Genetics*, 21(1), pp.52–57.

Rosicka, K., Mierzejewska-Krzyżowska, B. and Mrówczyński, W. (2022). Skin biomechanical and viscoelastic properties measured with MyotonPRO in different areas of human body. *Skin Research and Technology*, 28(2), pp.236–245.

Rosson, J., Egan, J., Shearer, J. and Monro, P. (1991). Bone weakness after the removal of plates and screws cortical atrophy or screw holes?. *The Journal of Bone and Joint Surgery*, 73(2), pp.283–286.

Ruffoni, D. and Van Lenthe, G.H. (2017). 3.10 Finite element analysis in bone research: A computational method relating structure to mechanical function. In: *Comprehensive Biomaterials II*. Elsevier, pp.169–196.

Saffar, K.P., Jamilpour, N. and Rajaai, S.M. (2009). How Does The Bone Shaft Geometry Affect its Bending Properties?. *American Journal of Applied Sciences*, 6(3), pp.463–470.

Sasajima, S., Yasuda, A., Kosaka, T. and Kubo, K. (2022). Effect of relaxation time on hysteresis of human tendon in vivo. *Journal of Musculoskeletal and Neuronal Interactions*, 2022, pp.1–6.

Schneebeli, A., Falla, D., Clijsen, R. and Barbero, M. (2020). Myotonometry for the evaluation of Achilles tendon mechanical properties: A reliability and construct validity study. *BMJ Open Sport and Exercise Medicine*, 6(1), pp.1–7.

Semb, H. (1966). The Breaking Strength of Normal and Immobilized Cortical Bone from Dogs. *Acta Orthopaedica Scandinavica*, 37(2), pp.131–140.

Silva, M.J., Eekhoff, J.D., Patel, T., Kenney-Hunt, J.P., Brodt, M.D., Steger-May, K., Scheller, E.L. and Cheverud, J.M. (2019). Effects of High-Fat Diet and Body Mass on Bone Morphology and Mechanical Properties in 1100 Advanced Intercross Mice. *Journal of Bone and Mineral Research*, 34(4), pp.711–725.

Sopakayang, R. and De Vita, R. (2011). A mathematical model for creep, relaxation and strain stiffening in parallel-fibered collagenous tissues. *Medical Engineering and Physics*, 33(9), pp.1056–1063.

Subramanian, A., Kanzaki, L.F., Galloway, J.L. and Schilling, T.F. (2018). Mechanical force regulates tendon extracellular matrix organization and tenocyte morphogenesis through TGFbeta signaling. *eLife*, 7, pp.1–24.

Synek, A., Ortner, L. and Pahr, D.H. (2023). Accuracy of osseointegrated screw-bone construct stiffness and peri-implant loading predicted by homogenized FE models relative to micro-FE models. *Journal of the Mechanical Behavior of Biomedical Materials*, 140, p.105740.

Thornton, G.M., Shrive, N.G. and Frank, C.B. (2001). Altering ligament water content affects ligament pre-stress and creep behaviour. *Journal of Orthopaedic Research*, 19(5), pp.845–851.

Torniainen, J., Ristaniemi, A., Sarin, J.K., Mikkonen, S., Afara, I.O., Stenroth, L., Korhonen, R.K. and Töyräs, J. (2019). Near Infrared Spectroscopic Evaluation of Ligament and Tendon Biomechanical Properties. *Annals of Biomedical Engineering*, 47(1), pp.213–222.

Valeri, C., Aloisio, A., Quinzi, V., di Stefano, G. and Marzo, G. (2024). Characterizing orthodontic mini-screws in the hard palate of pigs: An experimental and finite-element study. *Heliyon*, 10(3), p.e24952.

Vallefuoco, R., Pommellet, H. Le, Savin, A., Decambron, A., Manassero, M., Viateau, V., Gauthier, O. and Fayolle, P. (2016). Complications of appendicular fracture repair in cats and small dogs using locking compression plates. *Veterinary and Comparative Orthopaedics and Traumatology*, 29(1), pp.46–52.

Velkes, S., Nerubay, J. and Lokiec, F. (1966). Stress fracture of the proximal femur after screw removal. *Archives of Orthopaedic and Trauma Surgery*, 115, pp.61–62.

Vezzoni, L., Abrescia, P. and Vezzoni, A. (2021). Internal Radioulnar Fixation for Treatment of Nonunion of Proximal Radius and Ulna Fractures in a Toy Breed Dog. *VCOT Open*, 04(01), pp.e24–e31.

Vijayalakshmi, P., Veereshi, A., P Jayade, V., Dinesh, M. and Kumar, M. (2012). Finite Element Analysis of Stress and Strain Distribution in the Bone around the Implants used for Orthodontic Anchorage. *The Journal of Indian Orthodontic Society*, 46, pp.175–182.

Wadugodapitiya, S., Sakamoto, M., Suzuki, S., Morise, Y. and Kobayashi, K. (2021). In vivo stiffness assessment of patellar and quadriceps tendons by strain ultrasound elastography. *Bio-Medical Materials and Engineering*, 32(5), pp.257–266.

Wang, J., Zhang, X., Li, S., Yin, B., Liu, G., Cheng, X. and Zhang, Y. (2020). Plating System Design Determines Mechanical Environment in Long Bone Mid-shaft Fractures: A Finite Element Analysis. *Journal of Investigative Surgery*, 33(8), pp.699–708.

Wang, J.H.C., Guo, Q. and Li, B. (2012). Tendon biomechanics and mechanobiology - A minireview of basic concepts and recent advancements. *Journal of Hand Therapy*, 25(2), pp.133–141.

Welch, J.A., Boudrieau, R.J., De Jardin, L.M. and Spodnick, G.J. (1997). The Intraosseous Blood Supply of the Canine Radius: Implications for Healing of Distal Fractures in Small Dogs. *Veterinary Surgery*, 26, pp.57–61.

Wheatley, M.G.A., Rainbow, M.J. and Clouthier, A.L. (2020). Patellofemoral Mechanics: a Review of Pathomechanics and Research Approaches. *Current Reviews in Musculoskeletal Medicine*, 13(3), pp.326–337.

Yamazaki, T., Matsuura, Y., Nimura, A., Horiuchi, S., Suzuki, T. and Ohtori, S. (2021). Prediction of Stress Distribution Applied to the Triangular Fibrocartilage Complex: A Finite Element Analysis. *Journal of Hand Surgery Global Online*, 3(2), pp.94–98.

Yoo, J., Ma, X., Lee, J. and Hwang, J. (2021). Research Update on Stress Riser Fractures. *Indian Journal of Orthopaedics*, 55(3), pp.560–570.

Young, F.C., Cristi-Sánchez, I., Danes-Daetz, C., Monckeberg, J.E. and Aguirre, R.S. (2018). Patellar Tendon Stiffness in Elite Breakdancers Assessed by Myotonometric Measurement. *Journal of dance medicine & science : official publication of the International Association for Dance Medicine & Science*, 22(4), pp.179–183.

Yu, J., DeCamp, C.E. and Rooks, R. (2010). Improving surgical reduction in radial fractures using a ‘dowel’ pinning technique in miniature and toy breed dogs. *Veterinary and Comparative Orthopaedics and Traumatology*, 24(1), pp.45–49.

Zaki, M.E., Azab, A.A., Yousef, W., Wassal, E.Y. and El-Bassyouni, H.T. (2015). Cross-sectional analysis of long bones in a sample of ancient Egyptians. *Egyptian Journal of Radiology and Nuclear Medicine*, 46(3), pp.675–681.

Zapata, E., Rongieras, F., Pialat, J.B., Follet, H. and Mitton, D. (2017). An ex vivo experiment to reproduce a forward fall leading to fractured and non-fractured radii. *Journal of Biomechanics*, 63, pp.174–178.

Zapata, I., Lilly, M.L., Herron, M.E., Serpell, J.A. and Alvarez, C.E. (2022). Genetic testing of dogs predicts problem behaviors in clinical and nonclinical samples. *BMC Genomics*, 23(1), pp.1–19.

Zhang, G., Xu, S., Yang, J., Guan, F., Cao, L. and Mao, H. (2018). Combining specimen-specific finite-element models and optimization in cortical-bone material characterization improves prediction accuracy in three-point bending tests. *Journal of Biomechanics*, 76, pp.103–111.

Zhang, J., Li, H., Zhou, Y., Chen, S. and Rong, Q. (2023). An Analysis of Trabecular Bone Structure Based on Principal Stress Trajectory. *Bioengineering*, 10(10), pp.1–12.

Zhou, S., Jung, S. and Hwang, J. (2019). Mechanical analysis of femoral stress-riser fractures. *Clinical Biomechanics*, 63, pp.10–15.

Zink, C. and Schlehr, M.R. (2020). Working Dog Structure: Evaluation and Relationship to Function. *Frontiers in Veterinary Science*, 7, pp.1–12.